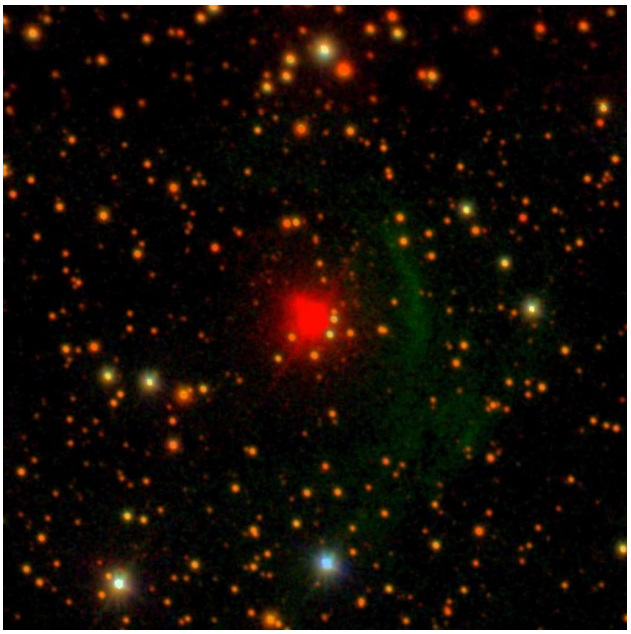

3D Radiative Transfer Modeling of the Red Supergiant NML Cyg

Master's thesis in Physics

PER HIRVONEN

DEPARTMENT OF SPACE, EARTH AND ENVIRONMENT

CHALMERS UNIVERSITY OF TECHNOLOGY
Gothenburg, Sweden 2021
www.chalmers.se

Master's thesis 2021

3D Radiative Transfer Modeling of the Red Supergiant NML Cyg

PER HIRVONEN

CHALMERS
UNIVERSITY OF TECHNOLOGY

Department of Space, Earth and Environment
Division of Astronomy and Plasma Physics
Evolved Stars group
Chalmers University of Technology
Gothenburg, Sweden 2021

3D Radiative Transfer Modeling of the Red Supergiant NML Cyg
PER HIRVONEN

Supervisors:
Dr. Holly Andrews, Department of Space, Earth and Environment
Dr. Elvire De Beck, Department of Space, Earth and Environment

Examiner: Dr. Elvire De Beck, Department of Space, Earth and Environment

Master's Thesis 2021
Department of Space, Earth and Environment
Division of Astronomy and Plasma Physics
Evolved Stars group
Chalmers University of Technology
SE-412 96 Gothenburg
Telephone +46 31 772 1000

Cover: The red supergiant NML Cyg, as viewed by the Sloan Digital Sky Survey Data Release 9. Original available through
http://skyserver.sdss.org/dr9/en/tools/chart/chart.asp?ra=311.60644046&dec=40.11654559

Typeset in LaTeX
Gothenburg, Sweden 2021

3D Radiative Transfer Modeling of the Red Supergiant NML Cyg
Per Hirvonen
Department of Space, Earth and Environment
Chalmers University of Technology

Abstract

Red supergiants are bright but cool massive stars that have depleted their core hydrogen supply and have started fusing heavier elements. These evolved stars experience a strong mass loss through a slow moving stellar wind that results in an extended circumstellar envelope with a rich chemistry. The circumstellar envelopes of red supergiants will eventually enrich the interstellar medium, influencing the formation and evolution of the next generation of stars and planets. Understanding the mass loss of massive evolved stars is a key component in understanding both the evolution of individual stars and the chemical evolution of the universe.

We analyze carbon monoxide emission around the red supergiant NML Cyg observed with the ground based JCMT 15 meter and Onsala 20 meter telescopes, as well as the HIFI instrument aboard the Herschel Space Observatory. The line profiles have complex shapes, suggestive of multiple components in the stellar outflow. 3D radiative transfer modeling is used to recreate the observed line profiles. We conclude that it is possible to recreate the observed line profiles by using one spherical component and three directed outflows.

Keywords: NML Cyg, astrophysics, radiative transfer modeling, supergiants, circumstellar environments

Acknowledgements

First of all I would like to thank my supervisors Holly Andrews and Elvire De Beck for their tremendous support over the last few months. Your knowledge, patience, kindness and feedback have been invaluable. I would also like to thank the entire Evolved Stars group for allowing me to attend your weekly meetings. Listening in on your discussions about astronomy have been really inspiring and a highlight of my week during these unusual circumstances.

Per Hirvonen, Gothenburg, June 2021

Contents

List of Figures

List of Tables

1

Introduction

During the first few minutes after the Big Bang, hydrogen, helium and small amounts of lithium were formed. At present day, we have detected 94 naturally occurring elements. To explain the chemical enrichment of the universe we need to understand the formation, life and death of stars. This thesis aims to present work on the chemically rich outflows of the red supergiant NML Cyg by using radiative transfer models of carbon monoxide emission.

1.1 Evolved stars

Stellar populations are generally shown in a so called Hertzsprung–Russell (HR) diagram as seen in Fig 1.1. The HR diagram is a log-log plot of stellar luminosities versus the surface temperature. On the HR diagram, most stars fall on a diagonal line known as the Main Sequence (MS). Stars will spend most of their life on the MS, fusing hydrogen into helium. Once the hydrogen in the core is depleted both the surface temperature and luminosity will change as the star enters a new stage of its life. The initial, or Zero-Age Main Sequence (ZAMS), mass determines which evolutionary track a star will take.

For stars with initial masses $0.8\,M_\odot < M_{\mathrm{ZAMS}} < 8\,M_\odot$ the post-MS evolutionary path is relatively well understood: after the hydrogen in the stellar core is depleted the star is unable to initially fuse helium into heavier elements (Habing & Olofsson 2004). During this period the star moves to the right in the HR diagram and ascends the first giant branch (Habing & Olofsson 2004, p. 28). The inert core gains mass and the temperature rises until core helium burning is triggered in a "helium core flash". During the helium burning phase the star's luminosity decreases as it moves along the Horizontal Branch (Kippenhahn et al. 2012, p. 407). When the helium supply in the stellar core is depleted no more fusion will take place for the remainder of the star's life as it ascends the Asymptotic Giant Branch (AGB) (Habing & Olofsson 2004, p. 28). Hydrogen and helium burning take place in shells outside of the inert core, and AGB stars experience a strong mass loss in the range $10^{-8}\,M_\odot$ yr^{-1} to $10^{-4}\,M_\odot$ yr^{-1} sustained through a mechanism known as a dust driven wind (Höfner & Olofsson 2018). The standard approach when modeling AGB stars is to assume a constant spherically symmetric mass-loss rate (Höfner & Olofsson 2018). Once the star has shed most of its envelope, all that remains is a white dwarf (Kippenhahn et al. 2012, p. 418).

The post-MS evolution of massive stars, $M_{\mathrm{ZAMS}} > 8\,M_\odot$, is not as well understood. There exists a range of classifications of evolved massive stars such as lu-

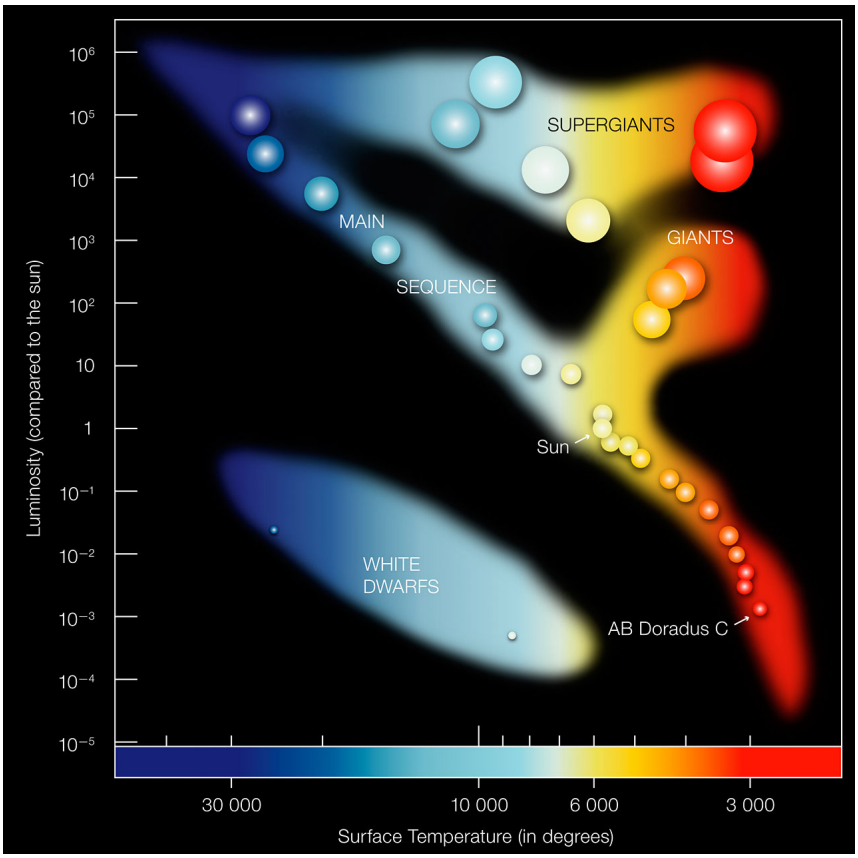

Figure 1.1: A schematic HR diagram showcasing the Main Sequence, a Giant Branch, a supergiant Branch and the area occupied by white dwarfs. The positions of the sun and the low mass star AB Doradus C are indicated. Original available through ESO (2007).

minous blue variables (LBVs), Wolf-Rayet (WR) stars, yellow hypergiants (YHGs) and red supergiants (RSGs). The classifications of massive evolved stars are based on surface temperatures and luminosities, which are not necessarily indicative of any differences in internal structure. As massive stars evolve, they can move between the different classes. The relationship between the different classes of evolved massive stars and the order in which these stages are reached is however an open question.

The evolved states of massive stars can broadly be classified into either "hot types" or "cool types", with WRs and LBVs belonging to the former and the YHGs and RSGs belonging to the latter (Smith 2014). The initial mass of a star, M_{ZAMS}, is a dominating factor in determining stellar structure and evolution, but it is also necessary to consider mass loss during and after the MS. Massive stars experience a significant mass loss during their MS lifetime and lose up to half of their mass after they evolve off the MS (Levesque 2017, p. 1-3).

Wolf-Rayet stars are massive helium burning stars whose powerful stellar winds, which reach velocities $1000\,\mathrm{km\,s^{-1}}$, have stripped the stars of their hydrogen envelope, leaving the core exposed (Smith 2014). There exists a range of sub-classes of WR stars depending on which exact features are present in their spectra, e.g. WN stars with nitrogen features and WC with carbon features. WR stars have

luminosities on the order of $10^5\,L_\odot$ and stellar temperatures ranging from 3×10^4 K to 1.5×10^5 K, depending on which sub-class a certain star belongs to (Crowther 2007). The stellar spectra of WRs are interesting, instead of the narrow absorption lines seen in most other types of stars, the stellar spectra of WRs are dominated by broad emission lines (Crowther 2007). For a star to evolve into a WR it would require $M_{\mathrm{ZAMS}} > 25\,M_\odot$ and, due to mass loss, the typical mass of a WR is around $10\,M_\odot$ to $25\,M_\odot$ (Meynet & Maeder 2005; Crowther 2007).

Another evolutionary phase experienced by massive stars is the luminous blue variable stage. The luminosity of these stars is variable, and some experience eruptive mass loss events. For the LBV η Car there are estimates that one such event gave rise to a mass-loss rate of up to $\dot{M} = 1\,M_\odot\ \mathrm{yr}^{-1}$, ejecting $10\,M_\odot$ to $20\,M_\odot$ over just a few decades (Smith 2014). Quantitative estimates of LBV mass-loss rates are generally lower, and fall between $10^{-5}\,M_\odot\ \mathrm{yr}^{-1}$ to $10^{-4}\,M_\odot\ \mathrm{yr}^{-1}$ (Smith 2014).

The LBV class is rather diverse; stellar evolution models predict that $M_{\mathrm{ZAMS}} > 25\,M_\odot$ is required to evolve into an LBV (Smith 2014). Furthermore they generally have temperatures 10^4 K, luminosities above $10^5\,L_\odot$ while the stellar wind generally reaches terminal velocities between $100\,\mathrm{km\,s^{-1}}$ and $600\,\mathrm{km\,s^{-1}}$ (de Jager 1998; Smith 2014).

Yellow hypergiants are large, luminous, yellow stars showing one or more broad Hα emission components (de Jager 1998). YHGs typically have luminosities $2 \times 10^5\,L_\odot$ and surface temperatures in the range 4000 K to 6000 K (van Genderen et al. 2019). YHGs have extended atmospheres and dense circumstellar envelopes. They experience a strong mass loss, sometimes in the forms of large eruptions; in the year 2000 an eruption caused the mass-loss rate of ρ Cas to reach $3 \times 10^{-2}\,M_\odot\ \mathrm{yr}^{-1}$ (van Genderen et al. 2019). Stellar evolution modeling suggests that stars with $25\,M_\odot < M_{\mathrm{ZAMS}} < 60\,M_\odot$ become YHG at some point during their life (de Jager 1998). Furthermore de Jager (1998) suggested that all YHGs are post-RSGs based partly upon elemental abundances, stellar masses and the properties of the circumstellar envelope for various YHGs. More research is however needed in order to confirm or reject this hypothesis.

Stars with M_{ZAMS} ranging from $8\,M_\odot$ to $40\,M_\odot$ are expected to experience a red supergiant phase where a significant fraction of the expected mass loss takes place (Levesque 2017, chapter 1), with the most extreme RSGs subject to mass-loss rates $10^{-3}\,M_\odot\ \mathrm{yr}^{-1}$ (Smith 2014). There are no current theoretical predictions for mass-loss rates of RSG stars. However, the mass loss does seem to be neither symmetrical nor constant in time. The well studied RSG VY CMa has a complex circumstellar envelope with structures reminiscent of arcs, clumps, knots and spikes which indicate that there have been several localized ejections of mass due to active regions on the stellar surface (Smith et al. 2001; Humphreys et al. 2007). Recently, Humphreys et al. (2021) used Hubble Space Telescope observations of the innermost ejecta of the RSG VY CMa to estimate the ejection times of several clumps and correlate these to periods of extended variability in the historical luminosity curves spanning back to the mid 19th century.

In order to understand the evolutionary paths of massive stars, numerical models have been constructed. Stellar evolution models are very complex and take a large variety of physics into account, but even the most advanced codes have large

uncertainties associated with them; for massive stars the largest source of uncertainty is the mass-loss rate (Smith 2014). If the underlying mechanics behind the mass loss are not well understood, accurate predictions of evolution become increasingly difficult. Furthermore, the majority of stellar evolution codes cannot deal with eruptive or explosive mass-loss events, which are observationally confirmed (Smith 2014). Further complications arise when considering that up to 75% of massive stars are found in binary pairs that are close enough for either mass transfer to take place through Roche lobe overflows or for the stars to merge (Sana et al. 2012; Smith 2014). A Roche lobe overflow is a short lived event that occurs when the outer layers of the primary, more massive, star is located beyond the interior Lagrange point, L1, of the binary system. This causes the gravitational pull from the secondary star to drag matter away from the primary, causing an "instantaneous", relative to the nuclear burning timescales, transfer of a significant amount of mass (Smith 2014). Not only is this a very sudden type of mass loss for the primary star, the typical timescale for Roche lobe overflows is 10^4 yr, the secondary may also be affected due to the increase in mass over such a short timescale. To model the evolution of binary systems and fully explore the parameter space would be an enormous undertaking, consuming vast amounts of computational resources.

Another important property for a star is its metallicity, which is the abundance of elements heavier than helium. The overall metallicity of the universe changes over time as stars produce new elements and release these into the interstellar medium. The metallicity is an important parameter in various contexts, including star and planetary formation, stellar evolution, and the formation of interstellar dust. The metallicity also affects the mass distribution of new born stars, which determine which evolutionary track the stars will take, and the mass-loss rates of stars, which also affects the stellar evolution (Smith 2014).

In order to understand the chemical evolution of the universe the stellar outflows of massive stars need to be understood. The stellar outflows will at some point reach the interstellar medium and enrich it with the products of the different nuclear processes that take place in the interior of these massive stars. Understanding the mass loss of massive stars is also important in order to determine the future of these stars. At the very end of their life, massive stars become supernovae. Supernovae play an important role in the evolution of the universe, releasing massive amounts of energy in a short amount of time while at the same time creating new elements. Low mass RSGs dominates the observationally confirmed supernova progenitors (Levesque 2017, p. 1-3), and high mass RSGs are very likely to also become supernovae after having lived through some intermediary evolutionary state(s) (Levesque 2017, p. 8-7). Understanding RSGs is thus important when it comes to understanding the conditions that lead to supernovae explosions.

1.2 Aims

The aim of this thesis is to explain the use of a multi-dimensional radiative transfer code to investigate the multi-component outflow of a red supergiant, NML Cyg, in order to provide constraints on the geometry of the outflows and extended envelopes around this star. This work was complemented by the inclusion of long-wavelength

observations of CO emission lines towards NML Cyg from a number of radio and millimetre-wavelength telescopes, including archival data from Herschel and JCMT as well as new data from the OSO 20 m telescope.

An overview of the importance of CO from an observational perspective is given in Section 1.3, followed by a description of the observations of NML Cyg that will be utilized in this project in Section 1.4. The radiative transfer equation and the methods used to solve it and construct a model of NML Cyg in SHAPE are presented in Chapter 2. The results are presented and discussed in Chapters 3 and 4 respectively. Final conclusions and future possible avenues of study are summarized in Chapter 5.

1.3 Carbon monoxide

Carbon monoxide (CO) is a very useful molecule for astronomers. While hydrogen is the most abundant element in the circumstellar envelopes that form around AGB stars and RSGs, it is very difficult to observe in these environments. Carbon monoxide is easier to observe, it forms relatively easily, has a high resistance to photodissociation and is not very chemically reactive, four properties that make it suitable as a tool to investigate the density structure and kinematics around evolved stars (Teyssier et al. 2012; Höfner & Olofsson 2018). The rotational transitions between states with angular momentum quantum number J to $J-1$ are most often used by astronomers. These spectral lines have, among other things, been used to set up analytical expressions that can estimate the mass-loss rates of AGB stars and RSGs (De Beck et al. 2010). Furthermore, the ratio of ^{13}C to ^{12}C, which can be estimated by studying the line intensities of the ^{12}CO and ^{13}CO isotopologues, can be used to assess the chemical evolution and evolutionary state of stars (De Beck et al. 2010). The isotopologues of CO probe different areas due to differences in self-shielding efficiency and difference in optical depth effects, further increasing the usefulness of this molecule to astronomers (Bally & Langer 1982; De Beck et al. 2010).

1.4 Observations

In radio astronomy, a common way to present the intensity of an observed spectral line is through the antenna temperature, defined as $T_A = \frac{c^2}{2k_B\nu^2} I_\nu$, where c is the speed of light, k_B is the Boltzmann constant and I_ν is the specific intensity (see Section 2.1). We have opted to use the main-beam temperature, $T_{mb}\eta_{mb} = T_A$, since it is more practical to use with the modeling software SHAPE. The "main-beam efficiency", η_{mb}, is a telescope specific parameter related to antenna beam patterns.

The resolution of a telescope is often reported as the beam size θ_b, which is a measurement of the full width at half maximum (FWHM) of the main beam.

For further details about intensity scales and beam sizes in radio astronomy, see any textbook on the subject, e.g. Wilson et al. (2013).

1.4.1 OSO 20 m

The Onsala Space Observatory 20 m telescope is a radio telescope located about 50 km south of Gothenburg. This project uses unpublished CO $J = (1 - 0)$ data observed in February 2016 (Andrews & De Beck 2021). The beam size θ_b of the telescope as well as the rest frequency ν and energy of the upper energy level E_u for the observed transitions are tabulated in Table 1.1. The data reduction was performed with the use of CLASS in GILDAS, a software package for reduction of (sub-)millimeter radioastronomical data and XS, a software package specifically developed for the reduction and analysis of spectra from the OSO telescopes (Andrews & De Beck 2021). The data reduction includes steps such as baseline corrections through low order polynomials, conversion of the data from antenna temperatures, T_A to main-beam temperatures, T_{mb}, and re-adjusting of the frequency axis to correct for inconsistencies in channel separation (Andrews & De Beck 2021).

1.4.2 JCMT

The *James Clark Maxwell Telescope* (JCMT) is a submillimetre Hawaii based telescope with a 15 m primary mirror. The JCMT data used in this project were first published in De Beck et al. (2010). The data was obtained using the A, B, HARP, RxW(C) and RxW(D) heterodyne receivers in beam-switching mode and reduced using the package SPECX. The beam size θ_b of the telescope as well as the rest frequency ν and energy of the upper energy level E_u for the observed transitions are tabulated in Table 1.1. For further details about the sample and observations, see De Beck et al. (2010) and the references therein.

1.4.3 HIFI

The *Heterodyne Instrument for the Far Infrared* (HIFI) aboard the Herschel Space Observatory was used to observe CO rotational lines around NML Cyg using the double-beam switching mode of the instrument. The observations and data reduction process was first presented in Teyssier et al. (2012). The beam size θ_b of the telescope as well as the rest frequency ν and energy of the upper energy level E_u for the observed transitions are tabulated in Table 1.1.

Table 1.1: The full width at half max (FWHM) θ_b [arcsec], as reported by De Beck et al. (2010), Teyssier et al. (2012), and Andrews & De Beck (2021), for the CO rotational lines utilized in this project along side their rest frequencies, ν [GHz], and upper energy level E_u [K] (Müller et al. 2005).

Telescope	Observed line	θ_b [arcsec]	ν [GHz]	E_u [K]
OSO	^{13}CO(1 − 0)	33	110.2	5.3
	^{12}CO(1 − 0)	33	115.3	5.5
JCMT	^{13}CO(2 − 1)	20	220.4	15.9
	^{12}CO(2 − 1)	20	230.5	16.6
	^{12}CO(3 − 2)	14	345.8	33.2
	^{12}CO(4 − 3)	11	461.0	55.3
	^{12}CO(6 − 5)	8	691.5	116.2
HIFI	^{13}CO(6 − 5)	32.4	661.1	111.1
	^{12}CO(6 − 5)	30.9	691.5	116.2

2

Radiative Transfer Modeling

2.1 The Radiative Transfer Equation

The study of how light is affected by travelling through a medium is known as radiative transfer. The electromagnetic power radiating from a unit area in a small frequency interval $d\nu$ in direction $\hat{\boldsymbol{n}}$ at position $\boldsymbol{r}$ within some solid angle $d\Omega$ at time t is given by

$$I_\nu(\nu, \hat{\boldsymbol{n}}, \boldsymbol{r}, t)d\nu d\Omega \tag{2.1}$$

where I_ν is known as the specific intensity. In a vacuum the specific intensity is distance invariant.

Let us consider the one dimensional case, $\boldsymbol{r} = r\hat{r}$, with some slab of material in between the source and the observer. If we characterize the material with an absorption coefficient κ_ν and emission coefficient j_ν the rate of change in specific intensity after travelling a distance ds is

$$\frac{dI_\nu}{ds} = j_\nu - I_\nu\kappa_\nu, \tag{2.2}$$

where subscript ν indicates a photon frequency dependence. If we also introduce the optical depth τ_ν through its relation to the physical path s as

$$d\tau_\nu = \kappa_\nu ds \tag{2.3}$$

and the source function $S_\nu = \frac{j_\nu}{\kappa_\nu}$ we can rewrite (2.2) as

$$\frac{dI_\nu}{d\tau_\nu} = S_\nu - I_\nu, \tag{2.4}$$

which we can solve by using the integrating factor e^{τ_ν} in order to acquire the general form of the radiative transfer equation,

$$I_\nu(\tau_\nu) = I_\nu(0)e^{-\tau_\nu} + \int_0^{\tau_\nu} e^{-(\tau_\nu - \tau'_\nu)}S_\nu(\tau_\nu)d\tau_\nu. \tag{2.5}$$

It should be noted that solving (2.5) analytically is not possible in all but a few cases due to the difficulty of constructing a source function and predicting the optical depth. Solving the equation is however needed in order to construct models of e.g. stellar environments and compare these to observations. A multitude of codes do exist to solve the radiative transfer equation numerically, including codes for dealing with 3D geometries, anisotropic scattering, polarization and more.

2.2 Solving the radiative transfer equation

To solve the radiative transfer equation one is often required to use numerical methods and approximations. SHAPE (Ste□en et al. 2011) is an implementation of a ray-casting algorithm to solve the radiative transfer equation. Ray-casting is a process where a beam of light propagates through a computational grid. As the beam propagates through the grid, each grid cell absorbs or emits some light. While a ray-casting algorithm is in general less accurate than Monte-Carlo methods, ray-casting can be orders of magnitude faster (Ste□en & Koning 2021). For this project, which aims to explore a vast parameter space, a fast run-time is key.

A SHAPE-model consists of a 3D-mesh model, constructed through the use of built-in primitive geometric objects, i.e. spheres, tori and cubes, or through mathematical equations. All geometric properties needed to fully describe one of the primitive geometric objects can be altered individually. The primitive geometric objects can be molded into more complex shapes, e.g. creating spiral structures or bipolar outflows, through the use of a set of built-in modifiers. The physical properties of the individual geometric objects, such as densities, temperatures and velocity fields, can be set either through analytical expressions or imported from an external source.

After a SHAPE-model is constructed, the first step in solving the radiative transfer equation is to construct a 3D grid where each cell has homogeneous properties derived from the 3D-mesh. In order to do this SHAPE performs a check to see which grid cells overlap with the mesh model (Ste□en & Koning 2021). If a cell is only partially occupied by the 3D-mesh the algorithm "weights" the cell by calculating the fraction of the cell that is overlapping with the mesh in order to avoid aliasing e□ects in the final outputs (Ste□en & Koning 2021).

Once the grid is constructed the properties of the cells need to be determined, in particular the absorption and emission coe□cients κ_ν and j_ν. Early versions of SHAPE could not model molecular species, which led to the development of the now fully integrated plugin `shapemol` (Santander-García et al. 2015). `shapemol` calculates the absorption and emission coe□cients κ_ν and j_ν for molecular species, which are necessary to solve the radiative transfer equation, by using the Large Velocity Gradient (LVG) approximation.

One di□culty with solving the radiative transfer equation is that it is a global problem: the emission from all frequencies at each point can interact with every other point. The LVG approximation can be applied in order to create a more localized problem, greatly reducing the complexity. The basic assumption of the LVG approximation is the existence of a large velocity gradient, which will ensure that the emission from di□erent regions of the object is Doppler shifted to di□erent extents. This di□erence in Doppler shift ensures that the emission from di□erent regions can be handled separately from each other, turning our global system into several smaller, localized systems. The general formalism for the LVG approximation is described in Castor (1970), but the standard LVG results will depend only on four parameters: the number density n, the temperature T, the logarithmic velocity gradient $\varepsilon = \frac{\mathrm{d}v}{\mathrm{d}r}\frac{r}{v}$ and the product $X\frac{r}{v}$ where r is the distance to the central star, v is the velocity and X is the abundance of the studied species relative to H_2. In

addition to these parameters `shapemol` also requires the user to input a characteristic micro-turbulence δv and a telescope beam size θ_b. For the purposes of solving the radiative transfer equation using SHAPE and `shapemol`, the optical depth τ_{LVG} is proportional to δv (Santander-García et al. 2015). In a more physical sense, δv represents turbulent eddies of finite size that cause Doppler broadening in spectral lines (Hundt 1973).

In practice, calculating κ_ν and j_ν can be quite resource intensive even when utilizing the LVG approximation. In order to reduce the run-time `shapemol` utilizes pre-generated tables of κ_ν and j_ν along with either nearest-neighbour or linear interpolation to calculate values not directly available through the tables. Tables for ^{12}CO and ^{13}CO calculated by the creators of `shapemol` are available online, see Santander-García et al. (2015) for the details of how these tables were constructed.

Once the grid and the cell properties are set, the ray-casting commences. This is the most resource intensive part of the process. Once a beam, consisting of N spectral bands within some specified wavelength range, has emerged from the grid in the direction of the observer, a pixel is rendered on the final image (Ste□en & Koning 2021). When all beams have emerged from the grid, additional data products are generated. The output products that this project utilizes is a 2D image, which is used to check for obvious artefacts and aliasing, and the molecular line profiles which can be directly compared to observational data.

2.3 Constructing and iterating on the 3D-mesh model

Radiative transfer modeling has previously been used to reconstruct observed molecular lines for the RSG VY CMa (Ziurys et al. 2007). The authors found that the line profiles could be explained by a spherical wind component in combination with several directed outflow components. In order to reconstruct the single dish CO-lines for the RSG NML Cyg it is assumed that this would also be the case, based on the apparent presence of multiple components in the measured CO spectra.

In order to model NML Cyg, an expansion velocity profile, a density profile, and a temperature profile need to be specified. The expansion velocity, v_∞, is assumed to be constant for all components, both the spherical and the directed outflows; the densities are given as a $\rho(r) = \dot{M}\,(4\pi v_\infty r^2)^{-1}$ where $\dot{M}$ is the mass-loss rate. The temperature profile $T(r) = T_{e□}\,(r/R_\star)^{-0.7}$, where $R_\star$ is the stellar radius, is adopted from Ziurys et al. (2007).

The directed outflows are constructed as spherical sectors with opening angle φ, inner radius r_{inner} and outer radius r_{outer}. Each directed component is constructed as a separate mesh that overlaps with the spherical wind mesh, see Fig. 3.3. The directed outflows use the same velocity and temperature profiles as the spherical wind but with increased mass-loss rates, $\dot{M}$, and hence increased densities, $\rho(r)$. This means that there can be two di□erent 3D-meshes in each grid cell with di□erent physical properties. To simplify the implementation, rather than merging the two objects into one, SHAPE deals with two overlapping geometrical objects by performing two separate calculations (Ste□en & Koning 2021). This introduces some small

inaccuracy to the solution (Ste□en & Koning 2021), this is further discussed in Section 4.4.2.1.

The orientation of the cones are given by two angles Φ_x and Φ_y, illustrated in Fig. 2.1, which are the rotation about the x and y axis, respectively. SHAPE uses a left-handed coordinate system where the xy-plane corresponds to the plane of the sky, and the line of sight coincides with the z-axis. The main purpose of the positioning angles is to modulate the Doppler shift of the directed outflows. The Doppler shift is determined by the projected velocity along the line of sight and the resulting line profile will be insensitive to rotations about the z-axis. Due to this there is a high level of degeneracy when it comes to the two positioning angles. To simplify the modeling and avoid any possible confusion arising from the angle degeneracy, only one of the positioning angles will be used as free parameter for each component while the other is kept constant. Thus there are five free parameters per directed outflow: $\dot{M}$, r_{inner}, r_{outer}, φ and Φ_x or Φ_y.

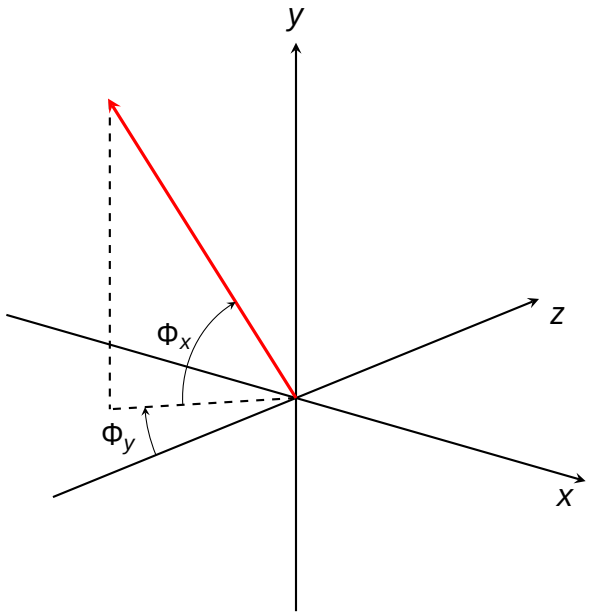

Figure 2.1: The left-handed coordinate system used by SHAPE. The z-axis coincides with the line of sight and the xy-plane corresponds to the plane of the sky. The positioning angle Φ_x corresponds to rotation about the x-axis in the yz-plane, and Φ_y coincides to a rotation about the y-axis in the xz-plane.

3

Results

Through an initial inspection of the data, using ^{12}CO $J = 2-1$ as the representative line, it was determined that three directed outflows were needed to reconstruct the lines in addition to a spherical wind component: one blueshifted moving towards the observer, one redshifted moving away from the observer and one component perpendicular to the line-of-sight. Due to limitations in how SHAPE deals with overlapping meshes, the positioning angles were set to ensure that the directed outflows do not overlap.

The fixed physical input parameters for the star and the stellar envelope can be found in Table 3.1. The micro-turbulence $\delta v = 2.5\,\mathrm{km\,s^{-1}}$ was set in accordance with Taniguchi et al. (2020). The expansion velocity v_∞ was set so that $v_\infty + \delta v = 33\,\mathrm{km\,s^{-1}}$. The value $33\,\mathrm{km\,s^{-1}}$ is the expansion velocity reported by De Beck et al. (2010), however adopting this value in conjunction with $\delta v = 2.5\,\mathrm{km\,s^{-1}}$ overestimated the width of the line profiles. To remedy this, the lower value $v_\infty = 30.5\,\mathrm{km\,s^{-1}}$ was adopted, see Section 4.4.3 for further details.

The ^{12}CO abundance, $X_{12} = 3 \times 10^{-4}$, is the result of a constraint imposed upon the model by the pre-computed $X\frac{r}{v}$ product that is utilized by `shapemol` to calculate the appropriate absorption and emission coefficients, κ_ν and j_ν. The adopted value is larger by a factor of 6 than the spherical outflow for VY CMa as modeled by Ziurys et al. (2007), and a factor of 3 higher than what De Beck et al. (2010) adopted for oxygen rich stars. The ^{13}CO abundance X_{13} is obtained from $X_{12}/X_{13} = 8.7$ as reported by De Beck et al. (2010).

A common assumption when carrying out radiative transfer modeling is that the radial expansion velocity is constant. However, the utilization of the LVG approximation requires a specification of the logarithmic velocity gradient ε, the available tables utilized by `shapemol` only allow for $\varepsilon > 0$. The model dependence on ε is very low compared to the other parameters (Santander-García et al. 2015). In order

Table 3.1: The fixed stellar properties used to model NML Cyg which include the expansion velocity v_∞ [km s^{-1}], characteristic micro-turbulence δv [km s^{-1}], the distance d [pc] to NML Cyg, the effective temperature T_{eff} [K], the stellar radius R [m], the abundances X for the CO isotopologues and the logarithmic velocity gradient ε. The distance, stellar radius and effective temperature are taken from De Beck et al. (2010). The rest of the fixed parameters are discussed in Chapter 3.

v_∞ [km s^{-1}]	δv [km s^{-1}]	d [pc]	T_{eff} [K]	R [m]	X_{12}	X_{13}	ε
30.5	2.5	1220 pc	3834	8.2×10^{11}	3×10^{-4}	3×10^{-5}	0.2

to minimize the discrepancy the lowest possible value allowed by the pre-computed tables, $\varepsilon = 0.2$, was utilized.

Through recent interferometric observations with the Northern Extended Millimeter Array (NOEMA) the outer radius of the envelope could be constrained to 5 , corresponding to $r_{\text{outer}} = 9 \times 10^{14}$ m $\approx 1100R$ at a distance of 1220 pc (Andrews 2021). The inner radius was set so that $r_{\text{inner,sphere}} \approx 50R$ or 4.0×10^{13} m. Several models were tested in order to confirm that including deeper regions of the envelope, i.e. reducing r_{inner}, had no impact on the ^{12}CO $J = 6 - 5$ lines. The inner radius is thus su□ciently small.

Mass-loss rate reported by De Beck et al. (2010), $\dot{M} = 8.7 \times 10^{-5} M_\odot$ yr^{-1}, resulted in intensities that were significantly overestimated for all lines when using only a spherical component with no directional outflows. Using a grid of mass-loss rates, ranging from $10^{-5} M_\odot$ yr^{-1} to $8 \times 10^{-5} M_\odot$ yr^{-1}, the mass loss of the spherical component was determined by picking a value that did not overestimate the intensity of any of the ^{12}CO lines. However, the $J = 6 - 5$ JCMT line was significantly more sensitive to the mass loss rates than the other lines. Adopting a mass-loss rate appropriate for $J = 6 - 5$ JCMT led to the rest of the lines being very weak without the addition of directed outflows. Additionally, all model configurations with three directed outflows that reproduced the remaining ^{12}CO lines overestimated the JCMT $J = 6 - 5$ intensity when compared to the observed data. To demonstrate this, and to demonstrate the degeneracy of the free parameters, two separate models were constructed, one with $\dot{M}_{\text{sphere, A}} = 3 \times 10^{-5} M_\odot$ yr^{-1} and one with $\dot{M}_{\text{sphere, B}} = 6 \times 10^{-5} M_\odot$ yr^{-1}. For further details on parameter degeneracy, see Section 4.4.1.

The parameters for the directed outflows were initially constrained using the ^{12}CO $J = 2 - 1$ line as it traces the full extent of the envelope. The ^{12}CO $J = 1 - 0$ also traces the full extent of the envelope, but there are clear signs of interstellar emission along the line of sight, which can be attributed to an interstellar clump (Andrews & De Beck 2021; Kemper et al. 2003). The $J = 1 - 0$ line is also a□ected by photodissociation in the outer regions of the outflow to a larger extent than the other CO lines, making it more dependent on external properties, rather than on the outflow properties themselves (De Beck et al. 2010). As the $J = 2 - 1$ line is free of contamination and is less sensitive to external influence, it was deemed more appropriate as a starting point for constraining the free parameters of the directed outflows.

The initial value of r_{inner} for the directed outflows was set equal to $r_{\text{inner, sphere}}$; the opening angles were set to $\varphi_{\text{initial}} = 10°$ and the mass-loss rates were set equal to that of the spherical component. The value of φ_{initial} was picked due to it producing clearly separated features while still being large enough to avoid aliasing and artefacts in the rendered image, which leads to unphysical features in spectral line profile.

Initial values for the positioning angles Φ_x and Φ_y for the directed components were then set by comparing the normalized line profiles of the observations and the model outputs. This was done in order to remove the need to set the mass-loss rates at this stage to any particular value. The positioning angles a□ect the Doppler shift of the emission, while the mass-loss rates a□ect the line intensity without causing any additional shift, see Fig. 3.1. As long as the mass-loss rates are high enough for the features in the spectra to be distinguishable the initial values for the positioning

angles can be set. After the initial positioning angles were set, the mass-loss rates and opening angles were tweaked.

Both the mass-loss rates and the opening angles increase the intensity of the component and alter the shape of the line profile, see Fig 3.1 and Fig. 3.2. It is evident that for a given opening angle, the intensity gained by increasing the mass-loss rate diminishes for higher and higher values. This is likely due to an optical depth e□ect: as more and more material is added, the optical depth increases and the inner regions become obscured, meaning that we no longer see all the added material, only the outer parts are visible. Narrow cones with high mass-loss rates are easy to fit to specific features, but can lead to deep notches in between the features that might not be present in the observed line profiles. They also necessitate very high mass-loss rates, and a model with opening angles φ 10° and $\dot{M}_{\text{sphere}}$ = $3 \times 10^{-5}\,M$ yr^{-1} might require $\dot{M}_{\text{directed}} > 10^{-3}\,M$ yr^{-1}, which is on the higher end of what is reported in the literature and would lead to the previously mentioned notches in the spectra. Having two overlapping 3D-meshes with vastly di□erent mass-loss rates also leads to increased uncertainties in the models, see Section 4.4.2.1. Wide cones have the opposite problem compared to the narrow ones, as they tend to blur the top of the line profiles, making it di□cult to recreate the observed data.

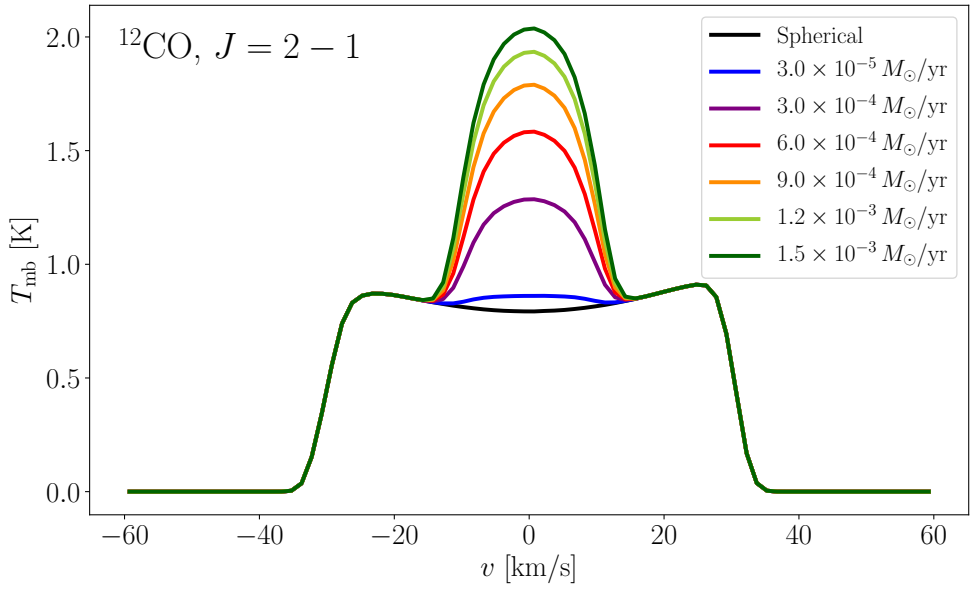

Figure 3.1: The impact of increasing the mass-loss rate, $\dot{M}$, of a directed component for the ^{12}CO $J = 2 - 1$ line intensity. The model consists of a directed outflow perpendicular to the line of sight, with $r_{\text{inner}} = 3 \times 10^{14}$ m, $r_{\text{outer}} = 9 \times 10^{14}$ m, $\varphi = 20°$ and $\Phi_x = 90°$, and a spherical component with $r_{\text{inner}} = 4 \times 10^{13}$ m, $r_{\text{outer}} = 9 \times 10^{14}$ m and mass-loss rate $\dot{M} = 3 \times 10^{-5}\,M$ yr^{-1}. The colored lines represent the line intensity when using di□erent mass-loss rates for the directed outflow. The solid black line is a reference model which includes only the spherical component.

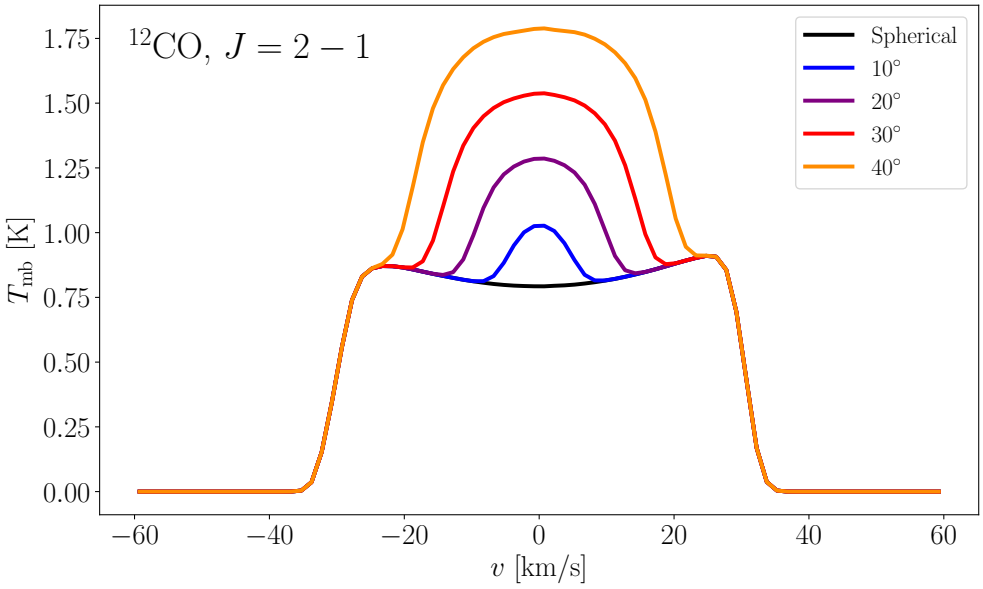

Figure 3.2: The impact of increasing the opening angle φ of a directed outflow component for the ^{12}CO $J = 2 - 1$ line intensity. The model consists of a directed component perpendicular to the line of sight, with $r_{\rm inner} = 3 \times 10^{14}$ m, $r_{\rm outer} = 9 \times 10^{14}$ m, $\Phi_x = 90°$ and mass-loss rate $\dot{M} = 3.0 \times 10^{-4}\, M_\odot$ yr^{-1}, and a spherical component with $r_{\rm inner} = 4 \times 10^{13}$ m, $r_{\rm outer} = 9 \times 10^{14}$ m and mass-loss rate $\dot{M} = 3 \times 10^{-5}\, M_\odot$ yr^{-1}. The colored lines represent the line intensity when using different opening angles φ for the directed outflow. The solid black line is a reference model which includes only the spherical component.

In order to get initial estimates for the last of the free parameters, the inner radii of the envelopes, the two $J = 6 - 5$ lines were studied as they only trace the innermost and hottest part of the modeled envelope. Using the same inner radii as the spherical component led to very intense lines, and the inner radii of the directed outflows were gradually increased until a good first fit was acquired.

Once initial values for all five free parameters for the three directed outflows had been constrained by studying the outer and innermost regions of the envelope, the intermediate excitation lines, $J = 3 - 2$ and $J = 4 - 3$ were assessed and the free parameters tweaked in order to improve the quality of the line profiles for these lines. This reduced the quality of the fit to the $J = 2 - 1$ and $J = 6 - 5$ lines; the best fit model were determined through an iterative process. Once no obvious improvements could be made by altering the free parameters, Model A was finalized. Fig. 3.3 shows two views of model A: one along the line of sight (head-on) and one of the xz-plane seen from above (bird's eye view). Model B was created by using the same positioning angles, inner and outer radii for the directed outflows as Model A, opting to only alter the opening angles φ.

We applied the same geometry to the available ^{13}CO lines to assess a first estimate on the possible structure traced by the isotopologue.

The best fit parameters for both models are displayed in Table 3.2 and the best fit

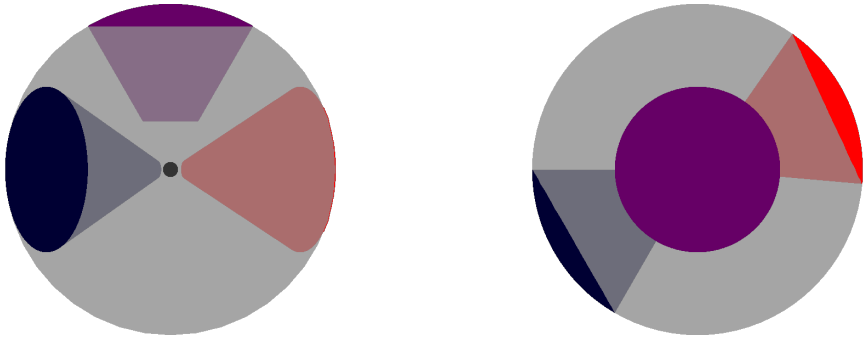

(a) Head-on (b) Bird's-eye

Figure 3.3: A head-on view and a bird's-eye view a of Model A as seen in SHAPE. The grey circle corresponds to the spherical component, the blue, red and purple segments correspond to the blueshifted, redshifted and central directed outflows. The small dark spot visible in the center of Figure 3.3a corresponds to the deepest region that is not modeled in this project.

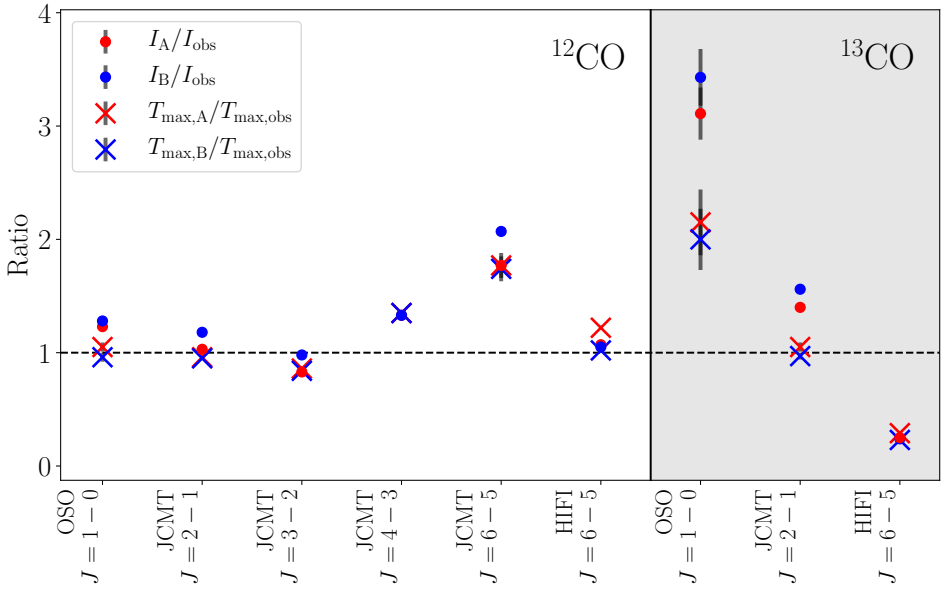

Figure 3.4: The ratios between the observed and modeled lines' peak and integrated intensities, $\frac{T_{max,\,model}}{T_{max,\,obs}}$ and $\frac{I_{model}}{I_{obs}}$, respectively. For the ^{12}CO and ^{13}CO $J = 1-0$ lines the interstellar contamination was removed prior to integration. The errors are taken as the root mean square (rms) of the observations, calculated from emission free regions and propagated through standard procedures. The exact values for the ratios can be found in Table 3.3

Table 3.2: The best fit parameters for the two radiative transfer models of NML Cyg consisting of a spherical component and three directed outflows. The parameters include the inner radii r_{inner} [m], the outer radii r_{outer} [m], the mass-loss rates $\dot{M}$ [$M_\odot$ yr^{-1}], the opening angles φ [deg] and the two positioning angles Φ_x [deg] and Φ_y [deg]. Note that depending on the convention used for v_∞ and δv the mass-loss rates might need scaling by a factor of $\eta = 1.1$ in order to reproduce the results presented in this thesis, see Section 4.4.3 for further details.

Component	r_{inner} [m]	r_{outer} [m]	$\dot{M}$ [$M_\odot$ yr^{-1}]	φ [deg]	Φ_x [deg]	Φ_y [deg]
Model A						
Spherical	4×10^{13}	9×10^{14}	3.0×10^{-5}			
Blue shift	1×10^{14}	9×10^{14}	1.5×10^{-4}	30	0	60
Red shift	1×10^{14}	9×10^{14}	2.1×10^{-4}	30	0	−115
Central	3×10^{14}	9×10^{14}	3.0×10^{-4}	30	90	0
Model B						
Spherical	4×10^{13}	9×10^{14}	6.0×10^{-5}			
Blue shift	1×10^{14}	9×10^{14}	1.5×10^{-4}	15	0	60
Red shift	1×10^{14}	9×10^{14}	2.1×10^{-4}	15	0	−115
Central	3×10^{14}	9×10^{14}	3.0×10^{-4}	20	90	0

^{12}CO line profiles compared to data, smoothed to a spectral resolution of $\Delta v_{\text{data}} = 3\,\text{km s}^{-1}$ to $4\,\text{km s}^{-1}$, can be seen in Figures 3.5, 3.6, 3.7, 3.8, 3.9 and 3.10 while the ^{13}CO profiles are displayed in Figures 3.11, 3.12 and 3.13. The peak and integrated intensities, T_{max} and I, as well as the ratios between the modeled and observed intensities, can be seen in Table 3.3. The intensity ratios are plotted in Fig. 3.4. All models have spectral resolution $\Delta v_{\text{model}} = 1.5\,\text{km s}^{-1}$ and velocity widths extending to $\pm 60\,\text{km s}^{-1}$, covering the full widths of the observed line profiles. The resolution was deemed sufficient in order to resolve the spectral features of the models.

The outer radii of the directed outflows were kept at the value constrained through the NOEMA data. Decreasing the outer radii mostly affects the $J = 1 - 0$ and $J = 2 - 1$ lines by decreasing their intensity, requiring higher mass-loss rates and opening angles. Since several of the higher excitation lines have very high intensities, this is adversarial. The $J = 1 - 0$ is also a good indicator that $r_{\text{outer, sphere}}$ is not too large, since this line is quite sensitive to this parameter. Using larger values quickly cause the $J = 1 - 0$ line to be overestimated even if the fit to the $J = 2 - 1$ line is good.

The three directed outflows all need to extend from the outermost part of the envelope and into regions just a few hundreds of stellar radii from the central star in order to recreate the observations. This is due to the fact that a spherical component alone cannot accurately recreate neither the low excitation lines nor the high excitation ones; no model with directed outflows that were significantly less extended could recreate the observed spectral lines.

Overall, the ^{13}CO lines are not as well explained by the model, and the main focus has been on the ^{12}CO lines. The ^{13}CO lines are further discussed in Section 4.1.4.

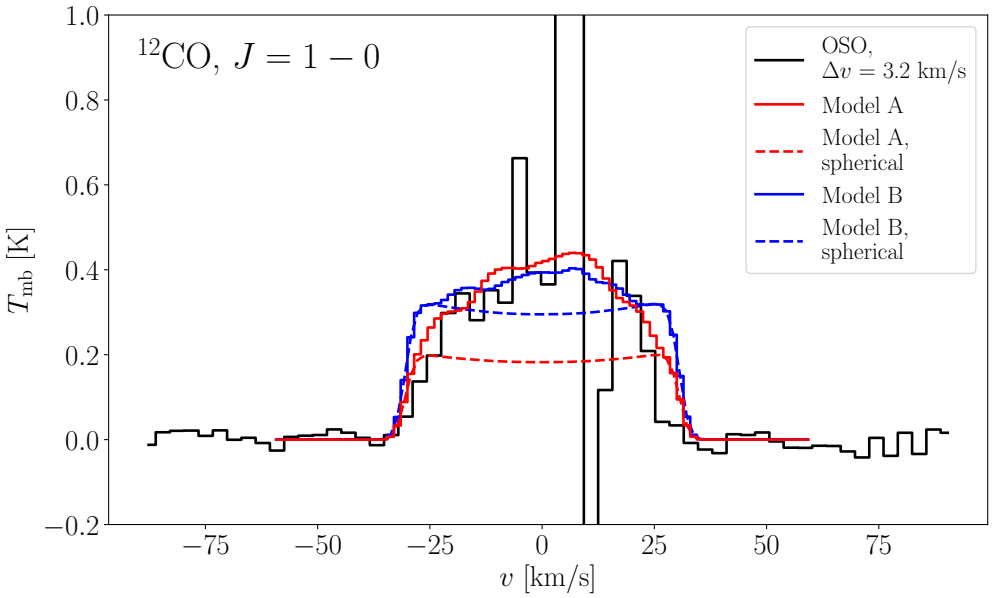

Figure 3.5: The smoothed ^{12}CO $J = 1 - 0$ line observed with OSO alongside the line profiles generated by SHAPE for Model A and Model B. The solid lines represent the full models, while the dashed lines correspond to the spherical components. The SHAPE model parameters can be found in Table 3.2. The spectral resolution of the model lines is $\Delta v = 1.5\,\mathrm{km\,s^{-1}}$.

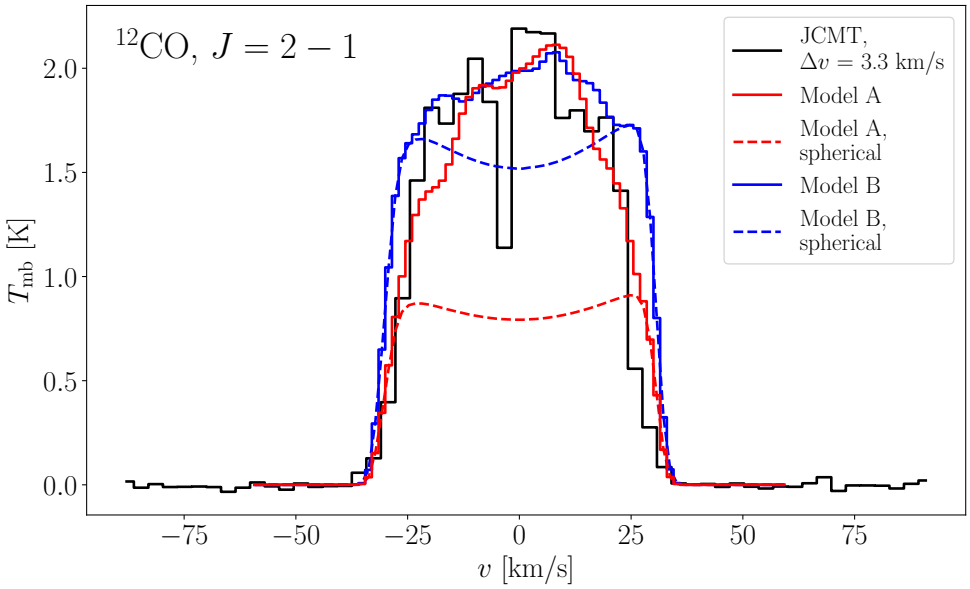

Figure 3.6: The smoothed ^{12}CO $J = 2 - 1$ line observed with JCMT alongside the line profiles generated by SHAPE for Model A and Model B. The solid lines represent the full models, while the dashed lines correspond to the spherical components. The SHAPE model parameters can be found in Table 3.2. The spectral resolution of the model lines is $\Delta v = 1.5\,\mathrm{km\,s^{-1}}$.

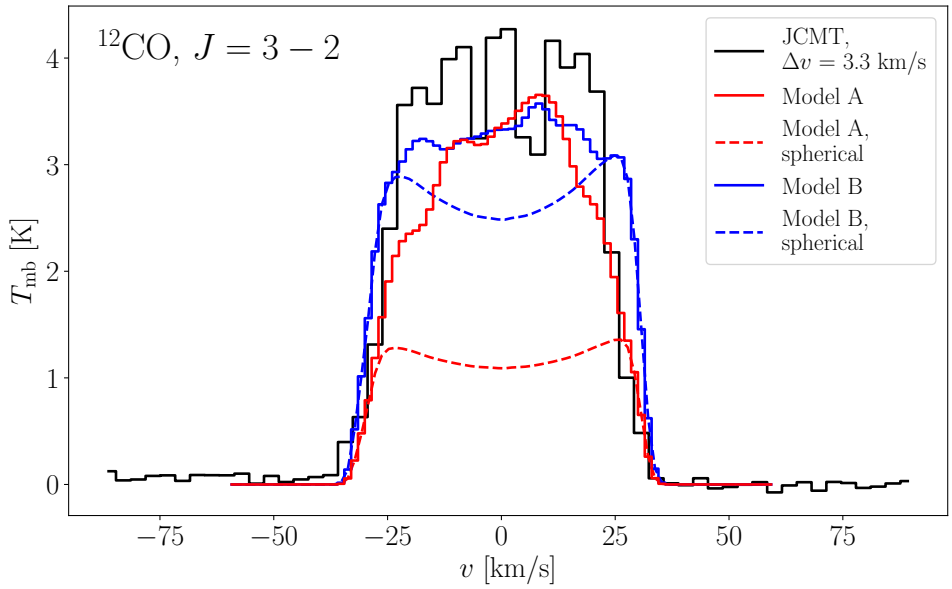

Figure 3.7: The smoothed ^{12}CO $J = 3 - 2$ line observed with JCMT alongside the line profiles generated by SHAPE for Model A and Model B. The solid lines represent the full models, while the dashed lines correspond to the spherical components. The SHAPE model parameters can be found in Table 3.2. The spectral resolution of the model lines is $\Delta v = 1.5\,\mathrm{km\,s^{-1}}$.

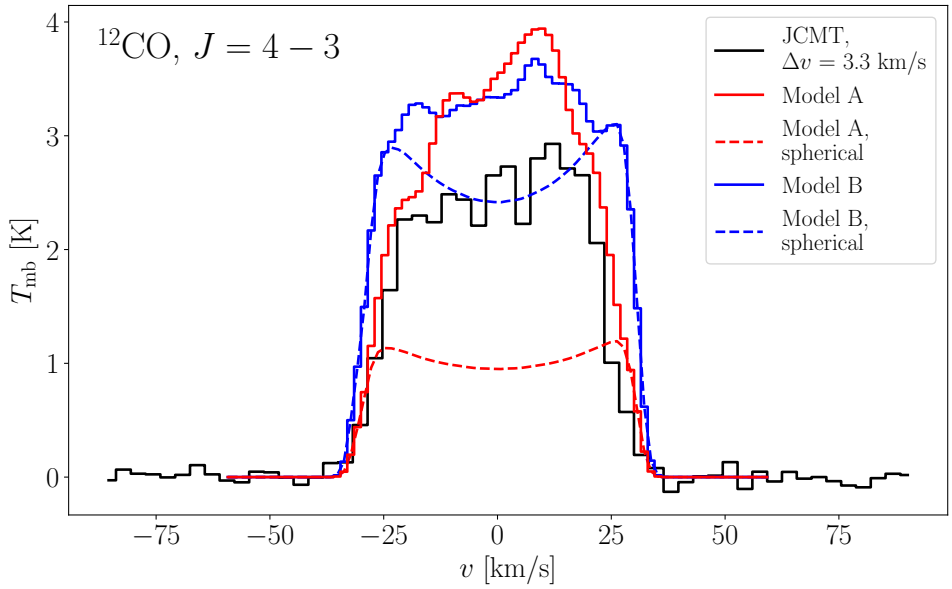

Figure 3.8: The smoothed ^{12}CO $J = 4 - 3$ line observed with JCMT alongside the line profiles generated by SHAPE for Model A and Model B. The solid lines represent the full models, while the dashed lines correspond to the spherical components. The SHAPE model parameters can be found in Table 3.2. The spectral resolution of the model lines is $\Delta v = 1.5\,\mathrm{km\,s^{-1}}$.

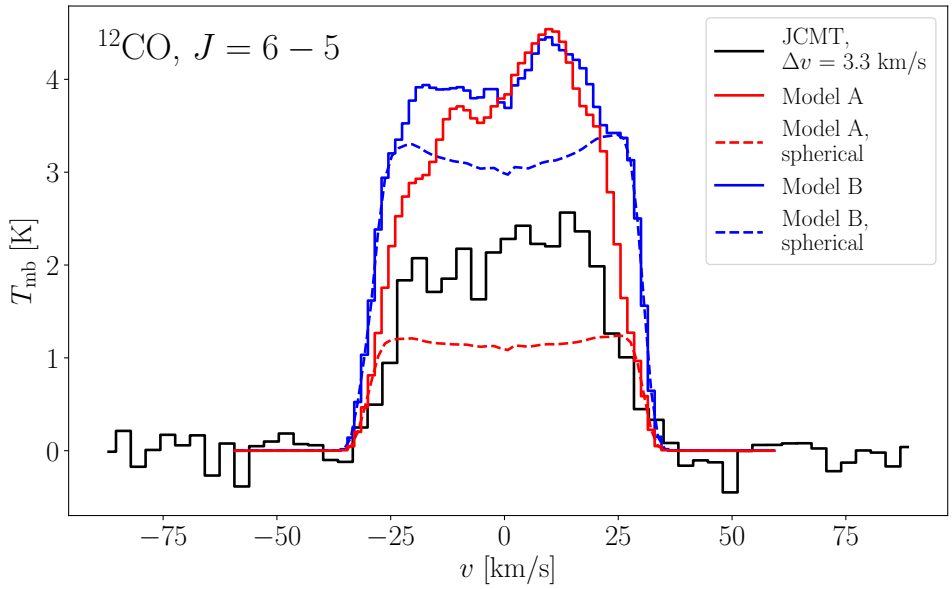

Figure 3.9: The smoothed ^{12}CO $J = 6 - 5$ line observed with JCMT alongside the line profiles generated by SHAPE for Model A and Model B. The solid lines represent the full models, while the dashed lines correspond to the spherical components. The SHAPE model parameters can be found in Table 3.2. The spectral resolution of the model lines is $\Delta v = 1.5\,\mathrm{km\,s^{-1}}$.

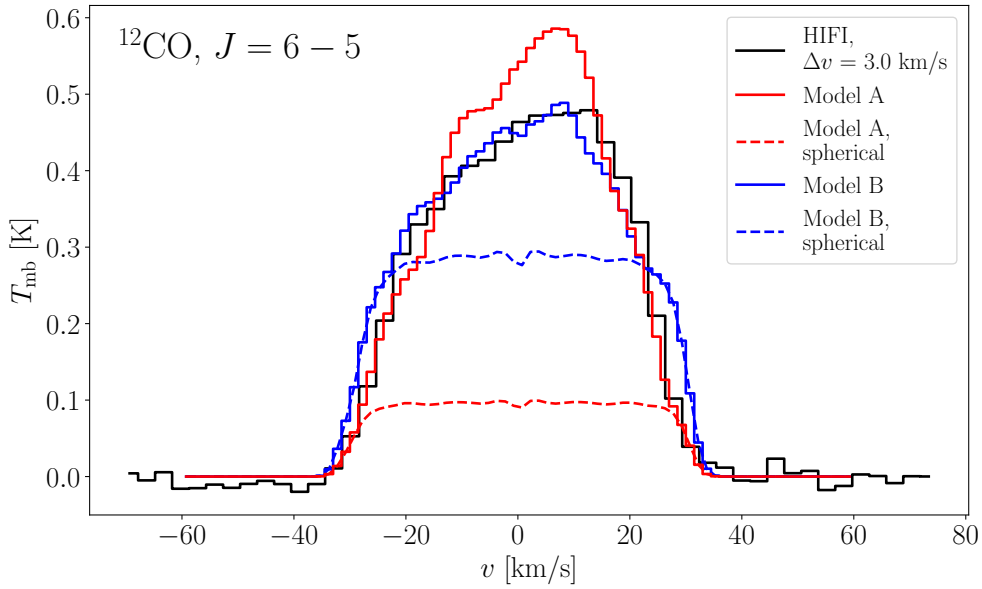

Figure 3.10: The smoothed ^{12}CO $J = 6 - 5$ line observed with HIFI alongside the line profiles generated by SHAPE for Model A and Model B. The solid lines represent the full models, while the dashed lines correspond to the spherical components. The SHAPE model parameters can be found in Table 3.2. The spectral resolution of the model lines is $\Delta v = 1.5\,\mathrm{km\,s^{-1}}$.

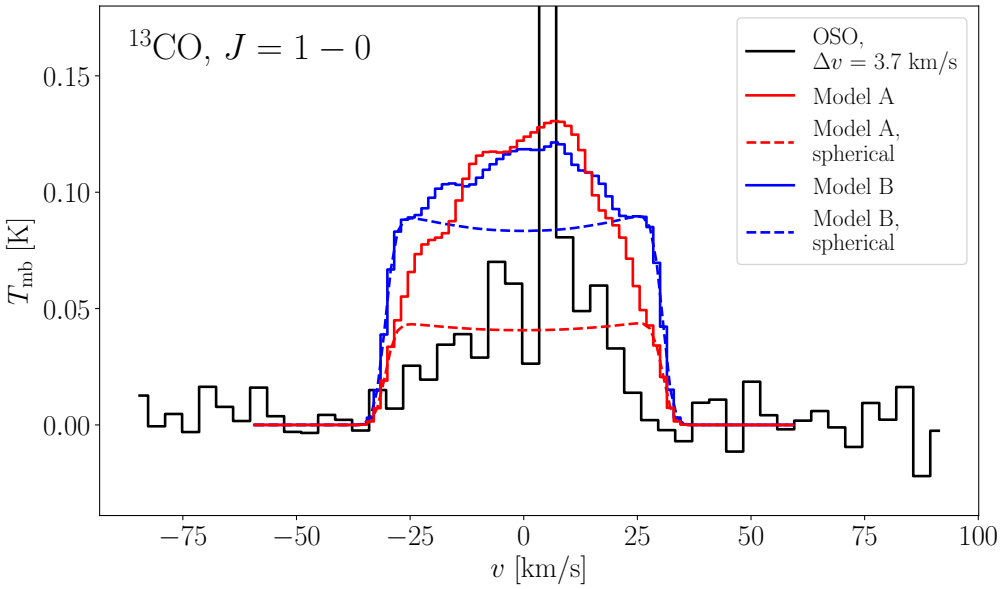

Figure 3.11: The smoothed ^{13}CO $J = 1 - 0$ line observed with OSO alongside the line profiles generated by SHAPE for Model A and Model B. The solid lines represent the full models, while the dashed lines correspond to the spherical components. The SHAPE model parameters can be found in Table 3.2. The spectral resolution of the model lines is $\Delta v = 1.5\,\mathrm{km\,s^{-1}}$.

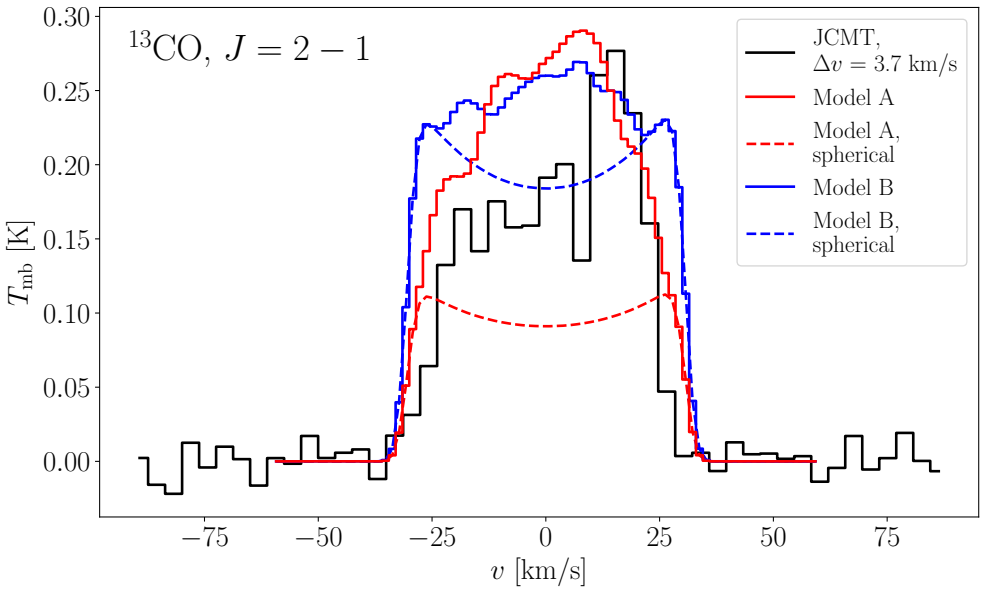

Figure 3.12: The smoothed ^{13}CO $J = 2 - 1$ line observed with JCMT alongside the line profiles generated by SHAPE for Model A and Model B. The solid lines represent the full models, while the dashed lines correspond to the spherical components. The SHAPE model parameters can be found in Table 3.2. The spectral resolution of the model lines is $\Delta v = 1.5\,\mathrm{km\,s^{-1}}$.

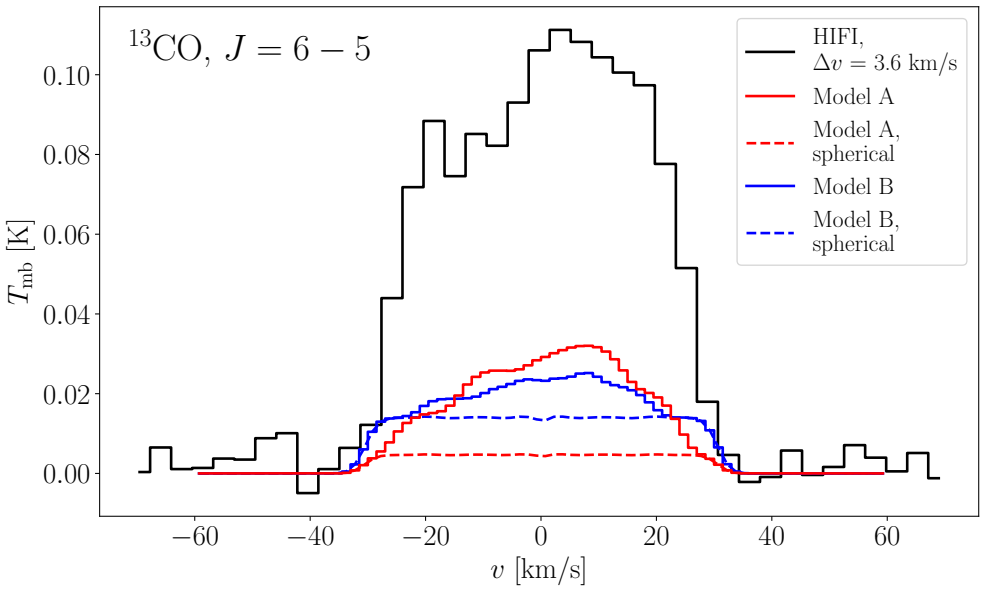

Figure 3.13: The smoothed ^{13}CO $J = 6 - 5$ line observed with HIFI alongside the line profiles generated by SHAPE for Model A and Model B. The solid lines represent the full models, while the dashed lines correspond to the spherical components. The SHAPE model parameters can be found in Table 3.2. The spectral resolution of the model lines is $\Delta v = 1.5\,\mathrm{km\,s^{-1}}$.

Table 3.3: The integrated intensity I [K km s^{-1}] and peak intensity T_{max} [K] for the observations, Model A and Model B for the different spectral lines, alongside the ratios $\frac{I_{\mathrm{model}}}{I_{\mathrm{obs}}}$ and $\frac{T_{\mathrm{max,\,model}}}{T_{\mathrm{max,\,obs}}}$. For the ^{12}CO and ^{13}CO $J = 1 - 0$ lines the interstellar contamination was removed prior to integration. The errors are listed as the root mean square (rms) of the observations, taken from emission free regions and propagated through standard procedures. The $\frac{I_{\mathrm{model}}}{I_{\mathrm{obs}}}$ and $\frac{T_{\mathrm{max,\,model}}}{T_{\mathrm{max,\,obs}}}$ ratios are illustrated in Fig. 3.4.

Spectral line	Data	I [K km s^{-1}]	$\frac{I_{\mathrm{model}}}{I_{\mathrm{obs}}}$	T_{max} [K]	$\frac{T_{\mathrm{max,\,model}}}{T_{\mathrm{max,\,obs}}}$
^{12}CO $J = 1 - 0$	OSO	16.94(26)		0.421(18)	
	Model A	20.77	1.226(19)	0.440	1.05(4)
	Model B	21.73	1.283(20)	0.404	0.96(4)
^{12}CO $J = 2 - 1$	JCMT	95.05(22)		2.190(14)	
	Model A	97.98	1.031(2)	2.113	0.96(1)
	Model B	112.60	1.185(3)	2.077	0.95(1)
^{12}CO $J = 3 - 2$	JCMT	198.32(79)		4.271(52)	
	Model A	164.91	0.832(3)	3.655	0.86(1)
	Model B	193.55	0.976(4)	3.573	0.84(1)
^{12}CO $J = 4 - 3$	JCMT	129.55(80)		2.929(51)	
	Model A	172.45	1.331(8)	3.942	1.35(2)
	Model B	195.54	1.509(9)	3.676	1.25(2)
^{12}CO $J = 6 - 5$	JCMT	110.47(239)		2.565(156)	
	Model A	195.99	1.774(38)	4.540	1.77(11)
	Model B	228.68	2.070(45)	4.453	1.74(11)
^{12}CO $J = 6 - 5$	HIFI	20.83(14)		0.479(9)	
	Model A	22.30	1.071(7)	0.586	1.22(2)
	Model B	21.93	1.053(7)	0.489	1.02(2)
^{13}CO $J = 1 - 0$	OSO	1.85(13)		0.061(8)	
	Model A	5.74	3.113(227)	0.131	2.15(29)
	Model B	6.32	3.426(250)	0.121	2.00(27)
^{13}CO $J = 2 - 1$	JCMT	9.52(15)		0.277(9)	
	Model A	13.31	1.398(22)	0.290	1.05(4)
	Model B	14.84	1.559(24)	0.269	0.97(3)
^{13}CO $J = 6 - 5$	HIFI	4.87(6)		0.111(4)	
	Model A	1.22	0.251(3)	0.032	0.29(1)
	Model B	1.16	0.239(3)	0.025	0.23(1)

4

Discussion

4.1 General discussion about the results

4.1.1 Quantitative measures of the model performance

It is evident that the model can reconstruct several lines, but the fits are not perfect and several lines have results that are very overestimated. Of these lines only three reproduce the integrated intensity within 20 % of the data, the ^{12}CO $J = 2 - 1$, $J = 3 - 2$ and $J = 6 - 5$ HIFI lines. It is worth noting that this is true for both Model A and Model B, see Table 3.3. The peak intensities that lie within 20 % for both models include the ^{12}CO $J = 1 - 0$, $J = 2 - 1$, and $J = 3 - 2$ lines, and the ^{13}CO $J = 2 - 1$ line. For the HIFI ^{12}CO J = 6 − 5 line, only Model B recreates the peak intensity within 20 % of the observed data.

Of the remaining lines, the worst fit with respect to integrated and peak intensity is the JCMT ^{12}CO $J = 6 - 5$ and the three ^{13}CO lines, with the exception of ^{13}CO $J = 2 - 1$ for the peak intensity. The overall shape of the ^{13}CO $J = 2 - 1$ is however not satisfactory, as it does not recreate any of the distinctive features, see Fig. 3.11. The results for the ^{13}CO lines are not surprising, as they were not part of the iterative modeling process.

With respect to the integrated and peak intensities, both models perform equally well, with maybe a slight advantage for Model B regarding the integrated intensities, I, and a slight advantage for Model A with respect to peak intensities, T_{max}. Since no best fit algorithm could be implemented, the results are subject to researcher bias. It is very likely that slight tweaks to any of the parameters on the orders of a few percent could have resulted in any of the models to perform better for any specific line.

4.1.2 Qualitative assessment of the line profiles

Overall, Model B with a higher $\dot{M}_{\mathrm{sphere}}$ and smaller opening angles φ does a better job recreating the top of the ^{12}CO line profiles, Model A on the other hand seems to follow the outer edges of the observed line profiles more precisely, recreating the width of the line profiles. It is possible that a third hypothetical model, with a mass loss in the range of $3 \times 10^{-5}\,M_\odot$ yr^{-1} to $6 \times 10^{-5}\,M_\odot$ yr^{-1} and opening angles in the range 15° to 30° could replicate both behaviours and lead to a better fit. This is however beyond the scope of this thesis.

4.1.3 The ^{12}CO, $J = 6 - 5$ lines

The $J = 6 - 5$ spectral line is the only one observed with two different telescopes, JCMT and HIFI. Recreating both observations with a single model is difficult. No parameter setup could be found that recreated the JCMT observation, with good integrated and peak intensities, that did not result in the rest of the lines being underestimated. This is not true for the HIFI observation. If one uses the geometrical setup for Model A but with lower mass-loss rates for the directed outflows in order to better recreate the ^{12}CO $J = 6 - 5$ JCMT line, the $J = 3 - 2$, $J = 2 - 1$ and $J = 1 - 0$ lines become weak. Increasing the inner radii of the directed outflows would reduce the emission of the $J = 6 - 5$ lines, but also reduce the intensities of both the $J = 4 - 3$ and $J = 3 - 2$ lines.

Due to the difficulties recreating the JCMT line, and as the HIFI observation has lower calibration uncertainties, the HIFI ^{12}CO $J = 6 - 5$ line was prioritised above the JCMT.

4.1.4 The ^{13}CO lines

All three ^{13}CO lines have different issues: the $J = 1 - 0$ line models greatly overestimate the intensity than the data, the $J = 2 - 1$ have a strong redshifted feature that is not accurately replicated in the model and the $J = 6 - 5$ model underestimate the intensity. These problems all point to the possibility that ^{13}CO trace different regions than ^{12}CO due to differences in optical depth. The optical depth is expected to be higher for ^{12}CO than for ^{13}CO due to the different abundances (De Beck et al. 2010). The higher optical depth for the ^{12}CO lines leave the deep layers of the circumstellar envelope more obscured when compared to the ^{13}CO lines.

It is possible that the X_{13} value is to high. The method used to determine the X_{12}/X_{13} ratio is based upon CO line intensity, and as such is only a first order estimate (De Beck et al. 2010). As mentioned in Section 3, the adopted ^{12}CO abundance is higher than what is found in the literature, which also leads to a higher ^{13}CO abundance. All in all, this would allow for a much lower value X_{13} value to be used. This would lead to a decrease in intensity for the ^{13}CO models. A full exploration of the effects of using a lower ^{13}CO abundance is beyond the scope of the project.

The $J = 2 - 1$ spectral line has a strong feature in the redshifted part of the spectra that lacks counterparts in the other observations. Altering the mass-loss rates of the model to recreate this feature would reduce the quality of the fit to the other lines. One possible alteration to the model would be the use of different chemical abundances for the different components, with the redshifted component having the highest ^{13}CO abundance of the three directed outflows. Using a range of abundances for different components has previously been explored by Ziurys et al. (2007) when modeling VY CMa.

In contrast with the ^{13}CO $J = 1-0$ and $J = 2-1$ lines, the ^{13}CO $J = 6-5$ models underestimate the emission. Decreasing the X_{13} value would have an adversarial effect on the fit to this line profile, leading to even lower emission. As with the ^{12}CO $J = 6 - 5$ lines, the ^{13}CO $J = 6 - 5$ intensity did not increase with a lower $r_{\text{inner, sphere}}$. Extending the directed outflows to reach deeper into the envelope would

increase the intensity, but would negatively affect the ^{12}CO $J = 6-5$ and $J = 4-3$ line fits.

4.2 Excluded high excitation CO lines

In addition to the ^{12}CO and ^{13}CO $J = 6-5$ lines, $J = 10-9$ and $J = 16-15$ were also observed with by HIFI (Teyssier et al. 2012). However, the limitations of the pre-computed tables used by `shapemol` prohibits the exploration of regions closer to the star than about $50R_*$. During the initial exploration of the mass loss of the spherical components $\dot{M}_{\rm sphere}$, attempts to model the $J = 10-9$ and $J = 16-15$ lines were unsuccessful. The resulting line profiles had intensities orders of magnitude lower than the data. Future modeling of these high excitation lines require software that is better suited to simulate the inner regions of the circumstellar envelope.

4.3 Comparison to VY CMa

Ziurys et al. (2007) used a different methodology when they performed radiative transfer modeling of the RSG VY CMa. The availability of high resolution Hubble Space Telescope images, which clearly display the morphology of the outer regions of the envelope, allow for constraints to be put on the geometrical layout of the model. Even if CO is not visible in the optical and infrared, the notion that CO is co-spatial with the dust that is generally visible in at shorter wavelengths is not uncommon. This allows for much greater constraints of the model, allowing for a more structured approach. While NML Cyg has been observed with Hubble, the observations only trace dust in a region much closer to the star than what is relevant for the CO lines modeled in this project (Schuster et al. 2009).

Ziurys et al. (2007) also assume a fixed mass-loss rate for their models, and opt instead to vary the abundances in order to recreate their observed lines. This is not possible to do within the constraints of this project, since the abundances are limited by the pre-computed $X\frac{r}{v}$ product.

Both approaches are valid, and share the same assumption: the mass-loss rates and abundances are independent of each other. It is necessary to make this assumption due to the lack of any current theoretical models about the formation of the stellar wind, and to reduce the computational resources needed to fully explore the parameter space.

4.4 The limitations of the model

Assuming a constant expansion velocity, the enhanced mass-loss events that formed the directed outflows must have lasted at least 600 to 800 years. Due to the directed outflows reaching all the way to the ^{12}CO dissociation radius, this is only a lower boundary. However, Humphreys et al. (2021) studied the historical light curves of the RSG VY CMa and concluded that the observed deep minima, which correlates to periods of increased mass loss, only lasted a few years. Since the two stars NML

Cyg and VY CMa are similar enough to warrant a comparison, a constant and long lasting increase in mass-loss rate is probably not an accurate description of the system. NML Cyg is a semi-regular variable with period 940 days (Schuster et al. 2009). As such, a more likely scenario might be the existence of several short lived outflows from NML Cyg with different mass-loss rates.

The assumption that the outflows can be described as perfect spherical sectors is also a simplification. Humphreys et al. (2007) lists over 50 distinct features reminiscent of knots, clumps, spikes and arcs present Hubble images around the RSG VY CMa; it would not be surprising to find something similar around NML Cyg. Using the level of detail presented in Humphreys et al. (2007) when constructing a radiative transfer model might not be necessary in order to recreate the main features of the observed spectral lines. Ziurys et al. (2007) managed to model VY CMa by using only two directed outflow components.

4.4.1 Parameter degeneracy

As evident by the similar quality of the two models, A and B, there is a high level of degeneracy between the parameters. In addition to the rotational invariance about an axis parallel to the line of sight through the origin, Fig. 3.1 and Fig. 3.2 illustrate two different ways to increase the intensity of the directed outflow components; by increasing the mass-loss rates $\dot{M}$ or by increasing the opening angles, φ. Empirically, using opening angles $15° \leq \varphi \leq 35°$ and mass-loss rates $1 \times 10^{-4}\,M_\odot\ \mathrm{yr}^{-1} \leq \dot{M} \leq 5 \times 10^{-4}\,M_\odot\ \mathrm{yr}^{-1}$ for the directed outflows were the most suitable to recreate the observed spectral lines. The most straight forward path to somewhat resolve this degeneracy is through constraining geometry of the directed outflows through spatially resolved observations. As previously mentioned, NOEMA recently observed NML Cyg (Andrews 2021). The use of these observations is however beyond the scope of this project.

The mass-loss rate of the spherical component, $\dot{M}_{\mathrm{sphere}}$, can also be varied to increase the overall intensity of the models, yielding another level of degeneracy. The strength of the spherical component relative to the directed outflows is related to the question about whether a constant, steady state wind is the main component of the mass loss, or if more short lived, localized events are. At the initial modeling of the spherical component, the JCMT observations of ^{12}CO $J = 6 - 5$ seemed as a promising line to use in order to put an upper constraint on the mass-loss rates as it seemed to be easier to overestimate than the rest of the ^{12}CO data. However, even when reconstructing the other lines within an upper tolerance 30 % the ^{12}CO JCMT $J = 6 - 5$ line was overestimated. We have no good explanation for this. The aforementioned spectral lines do have the largest errors, see Table 3.3, but the uncertainties are still too low to explain the discrepancy.

4.4.2 Error estimates

There are several sources of uncertainty in the modeling and model evaluation, many of them difficult to quantify. Some of them stem from the observations, e.g. the root-mean square (rms) errors and instrument specific limitations; some of them from

the difficulty of determining the physical parameters of NML Cyg, e.g. the effective temperature, stellar radii and the distance to the star; and some of them stem from the limitations of the software, e.g. the assumption of the LVG approximation in `shapemol`. As quantifying these errors is incredibly difficult, we opted to only include the rms when evaluating the models and the errors listed in Table 3.3 are thus conservative estimates.

4.4.2.1 Overlapping 3D-meshes in SHAPE

As noted in Section 2.3, SHAPE uses a simplified method to deal with overlapping 3D-meshes. This introduces some uncertainties in the models, which are difficult to quantify (Steffen & Koning 2021). Two of the main difficulties in quantifying these uncertainties from this approach is the geometrical setup and the inherent complexity of dealing with optical depth effects. A rough estimate might be acquired from studying a simple toy model, consisting of two geometrically identical spherical components, α and β, with radii $r_{\text{inner}} = 4 \times 10^{13}$ m, $r_{\text{outer}} = 9 \times 10^{14}$ m, and mass-loss rates $\dot{M}_\alpha = \gamma \times 10^{-4}\, M_\odot$ yr^{-1} and $\dot{M}_\beta = (1-\gamma) \times 10^{-4}\, M_\odot$ yr^{-1} with $0.5 \leq \gamma \leq 1$, respectively. The model is constructed so that, for all values of γ, $\dot{M}_\alpha + \dot{M}_\beta = 10^{-4}\, M_\odot$ yr^{-1}. Using $\gamma = 1$ corresponds to the use of a single spherical component with $\dot{M} = 10^{-4}\, M_\odot$ yr^{-1}, and $\gamma = 0.5$ corresponds to two completely identical spheres with $\dot{M}_\alpha = \dot{M}_\beta = 5 \times 10^{-3}\, M_\odot$ yr^{-1}. As γ increases the mass-loss rates, and thus the density profiles, of the two spheres grow less similar to each other. This setup should allow us to roughly quantify the uncertainties SHAPE introduces by performing two separate calculations, one for each object, rather of merging the two objects and performing one calculation.

The ratios $\frac{T_{\max}(\gamma)}{T_{\max}(\gamma=1)}$ and $\frac{I(\gamma)}{I(\gamma=1)}$ as a function of γ for ^{12}CO $J = 2-1$ is displayed in Fig. 4.1. It is evident that the intensities are underestimated when using two separate components as compared to a single component. As the spheres grow more dissimilar, the degree to which the models underestimate the intensities grows larger. It should be noted that the effect is most likely dependent on the total mass-loss rate of the two components, $\dot{M}_\alpha + \dot{M}_\beta$, and will vary between the spectral lines.

The largest γ value calculated from Table 3.2 is $\gamma = 0.9$, obtained by comparing the spherical with the central component for Model A. According to Fig. 4.1 this would make the resulting intensity underestimated by 6 %. However, this is assuming that the two components are geometrically identical. The actual error due to a single component is probably lower since the overlapping region is only fraction of the total volume. Due to the inherent difficulty and uncertainty when determining the model errors, they are excluded when calculating the uncertainties presented in Table 3.3.

4.4.3 A note on the expansion velocity

This work elected to use $v_\infty = 30.5\,\text{km s}^{-1}$, instead of the value found in the literature, $v_\infty = 33\,\text{km s}^{-1}$ (De Beck et al. 2010). When using the micro-turbulence $\delta v = 2.5\,\text{km s}^{-1}$ the resulting line profiles were always wider than the observed data. To remedy this, $v_\infty = 30.5\,\text{km s}^{-1}$ was adopted, since it recreated the width of the line profiles, and $v_\infty + \delta v = 33\,\text{km s}^{-1}$.

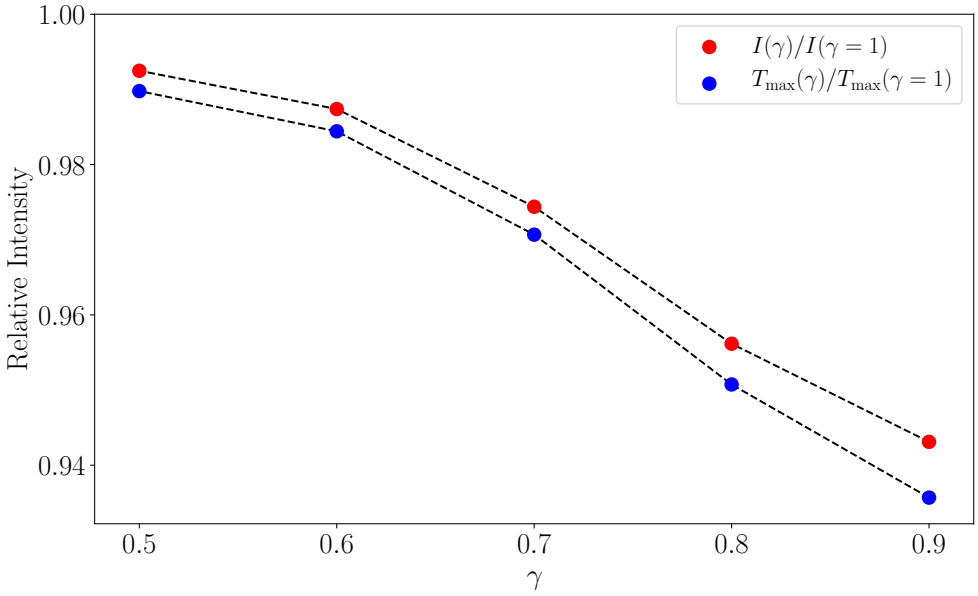

Figure 4.1: The ratio $\frac{I(\gamma)}{I(\gamma=1)}$ where $I(\gamma)$ corresponds to the integrated intensity of a toy model consisting of two geometrically, overlapping spherical components α and β, and $I(\gamma = 1)$ corresponds to using a single spherical component with total mass-loss $\dot{M} = \dot{M}_\alpha + \dot{M}_\beta$, for the ^{12}CO $J = 2-1$ line. The ratio $\frac{T_{\max}(\gamma)}{T_{\max}(\gamma=1)}$ is also displayed, where $T_{\max}(\gamma)$ is the peak intensity. The total mass-loss rate $\dot{M} = 10^{-4}\,M_\odot\ \mathrm{yr}^{-1}$, $r_{\mathrm{inner}} = 4 \times 10^{13}$ m and $r_{\mathrm{outer}} = 9 \times 10^{14}$ m.

The parameter v_∞ occurs on two separate occasions in the model: in the velocity field $v(r) = v_\infty$ and in the density distribution $\rho(r) = \dot{M}\,(4\pi v_\infty r^2)^{-1}$. In order to keep internal consistency we elected to use $v_\infty = 30.5\,\mathrm{km\,s^{-1}}$ for both $v(r)$ and $\rho(r)$. It is possible to adopt an alternative convention, using two parameters $v_{\infty,v} = 30.5\,\mathrm{km\,s^{-1}}$ and $v_{\infty,\rho} = 33\,\mathrm{km\,s^{-1}}$. In this case, the mass-loss rates of the model $\dot{M}$ needs to be scaled with a factor $\eta = 1.1$ in order to recreate the density distribution used in this work.

5

Conclusions and outlook

It is possible to use a four component model, consisting of a spherical component and three directed outflows, to recreate the detected ^{12}CO emission around the RSG NML Cyg by using radiative transfer modeling. It is not sufficient to only use a spherical component as the detailed features of the observed spectra cannot be recreated. Using fewer than three directed outflows would require very wide opening angles, leading to smearing of the line profiles and worse line profile fits that do not reproduce the details of the observations. The free parameters of the models are however degenerate and the reported values should only be taken as first estimates. There are some uncertainties regarding the mass-loss rates of the models due to how SHAPE handles overlapping geometrical objects. These uncertainties are expected to be low, but could be estimated by recreating Model A and Model B using a more complex radiative transfer implementation.

The great advantage of SHAPE is the interactive nature of the modeling; the ease of constructing and iterating upon 3D models. Translating the SHAPE models to a more complex and resource intensive code such as LIME (Brinch & Hogerheijde 2010) could yield further insights into the morphology of the stellar outflows as the use of a more complex software could allow for the study of the high excitation CO lines excluded from this work. A more complex software might also allow other molecular species to be studied and assess if they are co-spatial with CO. Alternatively, the construction of additional molecular tables in accordance with the requirements of shapemol would greatly extend the applicability of SHAPE.

The degeneracy of the geometric parameters of the directed outflows could be resolved through high resolution observations of the star. Spatially resolved observations would also open up the possibility to use channel maps which would greatly improve the quality of the model assessment. Channel maps are a set of heat maps, one for each spectral channel, that contains the spatial information of the observed emission. With channel maps the spatial structure is effectively resolved in 3 dimensions: two spatial dimensions and one spectral dimension. As mentioned in Section 3, NML Cyg has been observed with NOEMA which spatially resolves part of the envelope, however the observations only cover the $J = 2 - 1$ transitions of CO and are yet to be extensively analyzed (Andrews 2021).

The RSG μ Cep is less extreme than NML Cyg, with an estimated mass-loss rate $1 \times 10^{-6}\,M_\odot$ yr^{-1}, and has also been observed with NOEMA in the ^{12}CO $J = 2-1$ band (Montargès et al. 2019b). The 3D structure, which includes clumps rather than directed outflows, of the circumstellar envelope of μ Cep has been successfully investigated using 3D radiative transfer (Montargès et al. 2019a). Recreating the model of μ Cep with SHAPE could be useful in order to test the capabilities of the

software. Additionally, VY CMa, the most extensively studied RSG, would also be a good candidate for SHAPE modeling as there are plenty of observations constraining the geometry of the outflows. The 3D models of NML Cyg presented in this thesis can be directly tested and used as a starting point for future models of different stars.

Bibliography

Andrews, H. (May 2021). private communication.

Andrews, H. & De Beck, E. (2021). "The molecular content of supergiant outflows: Spectral survey of NML Cygni at 3mm and 4mm". in prep.

Bally, J. & Langer, W. D. (Apr. 1982). "Isotope-selective photodestruction of carbon monoxide." *ApJ* 255, pp. 143–148. DOI: 10.1086/159812.

Brinch, C. & Hogerheijde, M. R. (Nov. 2010). "LIME - a flexible, non-LTE line excitation and radiation transfer method for millimeter and far-infrared wavelengths". *A&A* 523, A25, A25. DOI: 10.1051/0004-6361/201015333.

Castor, J. I. (Jan. 1970). "Spectral line formation in Wolf-Rayet envelopes." *MNRAS* 149, p. 111. DOI: 10.1093/mnras/149.2.111.

Crowther, Paul A. (2007). "Physical Properties of Wolf-Rayet Stars". *Annual Review of Astronomy and Astrophysics* 45.1, pp. 177–219. DOI: 10.1146/annurev.astro.45.051806.110615.

De Beck, E., Decin, L., de Koter, A., et al. (Nov. 2010). "Probing the mass-loss history of AGB and red supergiant stars from CO rotational line profiles. II. CO line survey of evolved stars: derivation of mass-loss rate formulae". *A&A* 523, A18, A18. DOI: 10.1051/0004-6361/200913771.

de Jager, Cornelis (Jan. 1998). "The yellow hypergiants". *A&A Rev.* 8.3, pp. 145–180. DOI: 10.1007/s001590050009.

ESO (June 19, 2007). *Hertzsprung-Russell Diagram*. URL: https://www.eso.org/public/images/eso0728c/ (visited on 05/17/2021).

Habing, Harm J. & Olofsson, Hans (2004). *Asymptotic Giant Branch Stars. [electronic resource].* Astronomy and Astrophysics Library. Springer New York. ISBN: 9781475738766. URL: https://search.ebscohost.com/login.aspx?direct=true&AuthType=sso&db=cat07472a&AN=clec.SPRINGERLINK9781475738766&site=eds-live&scope=site&custid=s3911979&authtype=sso.

Höfner, S. & Olofsson, H. (Nov. 2018). "Mass loss of stars on the asymptotic giant branch". *The Astronomy and Astrophysics Review* 26.1, p. 1. ISSN: 0935-4956. DOI: 10.1007/s00159-017-0106-5.

Humphreys, Roberta M., Davidson, Kris, Richards, A. M. S., et al. (Mar. 2021). "The Mass-loss History of the Red Hypergiant VY CMa". *AJ* 161.3, 98, p. 98. DOI: 10.3847/1538-3881/abd316.

Humphreys, Roberta M., Helton, L. Andrew, & Jones, Terry J. (May 2007). "The Three-Dimensional Morphology of VY Canis Majoris. I. The Kinematics of the Ejecta". *The Astronomical Journal* 133.6, pp. 2716–2729. DOI: 10.1086/517609. URL: https://doi.org/10.1086/517609.

Hundt, E. (Nov. 1973). "Microturbulence in Stellar Spectroscopy". *A&A* 29, p. 17.

Kemper, F., Stark, R., Justtanont, K., et al. (Aug. 2003). “Mass loss and rotational CO emission from Asymptotic Giant Branch stars”. *A&A* 407, pp. 609–629. DOI: 10.1051/0004-6361:20030701.

Kippenhahn, Rudolf, Weigert, Alfred, & Weiss, Achim (2012). *Stellar Structure and Evolution. [electronic resource].* Astronomy and Astrophysics Library. Springer Berlin Heidelberg. ISBN: 9783642303043. URL: https://search.ebscohost.com/login.aspx?direct=true&AuthType=sso&db=cat07472a&AN=clec.SPRINGERLINK9783642303043&site=eds-live&scope=site&custid=s3911979&authtype=sso.

Levesque, Emily M (2017). *Astrophysics of Red Supergiants*. 2514-3433. IOP Publishing. ISBN: 978-0-7503-1329-2. DOI: 10.1088/978-0-7503-1329-2.

Meynet, G. & Maeder, A. (Jan. 2005). “Stellar evolution with rotation. XI. Wolf-Rayet star populations at different metallicities”. *A&A* 429, pp. 581–598. DOI: 10.1051/0004-6361:20047106.

Montargès, M., Homan, W., Keller, D., et al. (Dec. 2019a). “3D reconstruction of the environment of the red supergiant μCep from NOEMA observations of the CO v=0 J=2-1 line”. *SF2A-2019: Proceedings of the Annual meeting of the French Society of Astronomy and Astrophysics*. Ed. by P. Di Matteo, O. Creevey, A. Crida, et al., p. Di. URL: https://ui.adsabs.harvard.edu/abs/2019sf2a.conf..449M.

Montargès, M., Homan, W., Keller, D., et al. (May 2019b). “NOEMA maps the CO J = 2 - 1 environment of the red supergiant μ Cep”. *MNRAS* 485.2, pp. 2417–2430. DOI: 10.1093/mnras/stz397.

Müller, Holger S. P., Schlöder, Frank, Stutzki, Jürgen, & Winnewisser, Gisbert (May 2005). “The Cologne Database for Molecular Spectroscopy, CDMS: a useful tool for astronomers and spectroscopists”. *Journal of Molecular Structure* 742.1-3, pp. 215–227. DOI: 10.1016/j.molstruc.2005.01.027.

Sana, H., de Mink, S. E., de Koter, A., et al. (July 2012). “Binary Interaction Dominates the Evolution of Massive Stars”. *Science* 337.6093, p. 444. DOI: 10.1126/science.1223344.

Santander-García, M., Bujarrabal, V., Koning, N., & Steffen, W. (Jan. 2015). “SHAPE-MOL: a 3D code for calculating CO line emission in planetary and protoplanetary nebulae. Detailed model-fitting of the complex nebula NGC 6302”. *A&A* 573, A56, A56. DOI: 10.1051/0004-6361/201322348.

Schuster, M. T., Marengo, M., Hora, J. L., et al. (July 2009). “Imaging the Cool Hypergiant NML Cygni’s Dusty Circumstellar Envelope with Adaptive Optics”. *ApJ* 699.2, pp. 1423–1432. DOI: 10.1088/0004-637X/699/2/1423.

Smith, Nathan (2014). “Mass Loss: Its Effect on the Evolution and Fate of High-Mass Stars”. *Annual Review of Astronomy and Astrophysics* 52.1, pp. 487–528. DOI: 10.1146/annurev-astro-081913-040025.

Smith, Nathan, Humphreys, Roberta M., Davidson, Kris, et al. (Feb. 2001). “The Asymmetric Nebula Surrounding the Extreme Red Supergiant VY Canis Majoris”. *AJ* 121.2, pp. 1111–1125. DOI: 10.1086/318748.

Steffen, W. & Koning, N. (2021). *Physics in SHAPE*. URL: http://www.astrosen.unam.mx/shape/v4/downloads/files/Physics_in_SHAPE.pdf (visited on 04/14/2021).

Ste□en, Wolfgang, Koning, Nicholas, Wenger, Stephan, et al. (Apr. 2011). “Shape: A 3D Modeling Tool for Astrophysics”. *IEEE Transactions on Visualization and Computer Graphics* 17.4, pp. 454–465. DOI: 10.1109/TVCG.2010.62.

Taniguchi, Daisuke, Matsunaga, Noriyuki, Jian, Mingjie, et al. (Feb. 2020). “Effective temperatures of red supergiants estimated from line-depth ratios of iron lines in the YJ bands, 0.97-1.32μm”. *Monthly Notices of the Royal Astronomical Society* 502.3, pp. 4210–4226. DOI: 10.1093/mnras/staa3855.

Teyssier, D., Quintana-Lacaci, G., Marston, A. P., et al. (Sept. 2012). “Herschel/HIFI observations of red supergiants and yellow hypergiants. I. Molecular inventory”. *A&A* 545, A99, A99. DOI: 10.1051/0004-6361/201219545.

van Genderen, A. M., Lobel, A., Nieuwenhuijzen, H., et al. (Nov. 2019). “Pulsations, eruptions, and evolution of four yellow hypergiants”. *A&A* 631, A48, A48. DOI: 10.1051/0004-6361/201834358.

Wilson, Thomas L., Rohlfs, Kristen, & Hüttemeister, Susanne (2013). *Tools of radio astronomy.* Astronomy and astrophysics library. Springer. ISBN: 9783642399497.

Ziurys, L. M., Milam, S. N., Apponi, A. J., & Woolf, N. J. (June 2007). “Chemical complexity in the winds of the oxygen-rich supergiant star VY Canis Majoris”. *Nature* 447.7148, pp. 1094–1097. DOI: 10.1038/nature05905.

DEPARTMENT OF SPACE, EARTH AND ENVIRONMENT
CHALMERS UNIVERSITY OF TECHNOLOGY
Gothenburg, Sweden
www.chalmers.se

CHALMERS
UNIVERSITY OF TECHNOLOGY